



# High-resolution Near-infrared Spectroscopy of a Flare around the Ultracool Dwarf $\nu$ B 10

Shubham Kanodia<sup>1,2</sup> , Lawrence W. Ramsey<sup>1,2</sup> , Marissa Maney<sup>1,2</sup> , Suvrath Mahadevan<sup>1,2</sup> , Caleb I. Cañas<sup>1,2,21</sup> ,  
Joe P. Ninan<sup>1,2</sup> , Andrew Monson<sup>1,2</sup> , Adam F. Kowalski<sup>3,4,5</sup> , Maximos C. Goumas<sup>6</sup> , Gudmundur Stefansson<sup>7,22</sup> ,  
Chad F. Bender<sup>8</sup> , William D. Cochran<sup>9,10,11</sup> , Scott A. Diddams<sup>12,13</sup> , Connor Fredrick<sup>12,13</sup> , Samuel Halverson<sup>14</sup> ,  
Fred Hearty<sup>1,2</sup> , Steven Janowiecki<sup>10</sup> , Andrew J. Metcalf<sup>15</sup> , Stephen C. Odewahn<sup>9,10</sup> , Paul Robertson<sup>16</sup> , Arpita Roy<sup>17,18</sup> ,  
Christian Schwab<sup>19</sup> , and Ryan C. Terrien<sup>20</sup>

<sup>1</sup> Department of Astronomy & Astrophysics, 525 Davey Laboratory, The Pennsylvania State University, University Park, PA 16802, USA; [shbhuk@gmail.com](mailto:shbhuk@gmail.com)

<sup>2</sup> Center for Exoplanets and Habitable Worlds, 525 Davey Laboratory, The Pennsylvania State University, University Park, PA 16802, USA

<sup>3</sup> Department of Astrophysical and Planetary Sciences, University of Colorado Boulder, 2000 Colorado Ave., Boulder, CO 80305, USA

<sup>4</sup> National Solar Observatory, University of Colorado Boulder, 3665 Discovery Drive, Boulder, CO 80303, USA

<sup>5</sup> Laboratory for Atmospheric and Space Physics, University of Colorado Boulder, 3665 Discovery Drive, Boulder, CO 80303, USA

<sup>6</sup> Department of Aerospace, Physics, and Space Sciences, Florida Institute of Technology, Melbourne, FL 32901, USA

<sup>7</sup> Department of Astrophysical Sciences, Princeton University, 4 Ivy Lane, Princeton, NJ 08540, USA

<sup>8</sup> Steward Observatory, The University of Arizona, 933 N. Cherry Avenue, Tucson, AZ 85721, USA

<sup>9</sup> Department of Astronomy, The University of Texas at Austin, Austin, TX 79734, USA

<sup>10</sup> McDonald Observatory, The University of Texas at Austin, Austin, TX 79734, USA

<sup>11</sup> Center for Planetary Systems Habitability, The University of Texas at Austin, Austin, TX 79734, USA

<sup>12</sup> Time and Frequency Division, National Institute of Standards and Technology, 325 Broadway, Boulder, CO 80305, USA

<sup>13</sup> Department of Physics, University of Colorado, 2000 Colorado Avenue, Boulder, CO 80309, USA

<sup>14</sup> Jet Propulsion Laboratory, 4800 Oak Grove Drive, Pasadena, CA 91109, USA

<sup>15</sup> Space Vehicles Directorate, Air Force Research Laboratory, 3550 Aberdeen Ave. SE, Kirtland AFB, NM 87117, USA

<sup>16</sup> Department of Physics & Astronomy, University of California, Irvine, Irvine, CA 92697, USA

<sup>17</sup> Space Telescope Science Institute, 3700 San Martin Dr., Baltimore, MD 21218, USA

<sup>18</sup> Department of Physics and Astronomy, Johns Hopkins University, 3400 N. Charles Street, Baltimore, MD 21218, USA

<sup>19</sup> Department of Physics and Astronomy, Macquarie University, Balaclava Road, North Ryde, NSW 2109, Australia

<sup>20</sup> Department of Physics and Astronomy, Carleton College, One North College Street, Northfield, MN 55057, USA

Received 2021 August 31; revised 2021 November 23; accepted 2021 November 25; published 2022 February 2

## Abstract

We present high-resolution observations of a flaring event in the M8 dwarf  $\nu$ B 10 using the near-infrared Habitable-zone Planet Finder (HPF) spectrograph on the Hobby-Eberly Telescope. The high stability of HPF enables us to accurately subtract a  $\nu$ B 10 quiescent spectrum from the flare spectrum to isolate the flare contributions and study the changes in the relative energy of the Ca II infrared triplet, several Paschen lines, the He  $\lambda$ 10830 triplet lines, and to select iron and magnesium lines in HPF's bandpass. Our analysis reveals the presence of a red asymmetry in the He  $\lambda$ 10830 triplet, which is similar to signatures of coronal rain in the Sun. Photometry of the flare derived from an acquisition camera before spectroscopic observations and the ability to extract spectra from up-the-ramp observations with the HPF infrared detector enable us to perform time-series analysis of part of the flare and provide coarse constraints on the energy and frequency of such flares. We compare this flare with historical observations of flares around  $\nu$ B 10 and other ultracool M dwarfs and attempt to place limits on flare-induced atmospheric mass loss for hypothetical planets around  $\nu$ B 10.

*Unified Astronomy Thesaurus concepts:* [Stellar flares \(1603\)](#); [Optical flares \(1166\)](#); [Near infrared astronomy \(1093\)](#); [M stars \(985\)](#)

*Supporting material:* machine-readable table

## 1. Introduction

Stellar flares are a common phenomenon around M dwarfs. These transient events take place when magnetic field lines reconnect in the upper atmosphere of the star. This converts a large amount of magnetic energy to kinetic energy of electrons and ions, which is then redistributed across the electromagnetic spectrum. These nonthermal accelerated electrons collide with the cold, thick lower chromosphere and upper photosphere and

emit a white-light continuum, which is approximately a blackbody of temperature 10,000 K (Mochnacki & Zirin 1980; Kahler et al. 1982; Kowalski et al. 2015). This blackbody emission dominates in the blue/visible over the M dwarf continuum and is typically accompanied by high-energy X-ray and UV radiation.

Flares around M dwarfs have been studied photometrically since the 1940s (van Maanen 1940; Joy & Humason 1949), with the first spectroscopic observations following soon after (Herbig 1956). Kunkel (1970) presented a two-component spectral model consisting of hydrogen recombination similar to solar flares, as well as a second component that follows shortly after: an impulsive component that heats the photosphere. However, this model does not include the spectral features observed during flares such as line emission. While the continuum emission is typically that of a blackbody of

<sup>21</sup> NASA Earth and Space Science Fellow.

<sup>22</sup> Henry Norris Russell Fellow.



$\sim 10,000$  K, the emission lines can include H, He, and Ca ionic species at chromospheric temperatures.<sup>23</sup>

Studies of M dwarf flares using high-resolution spectroscopy are sparse owing to the challenges associated with their faintness, which is an even bigger problem for ultracool dwarfs. High resolving power ( $R \sim 110,000$ ) spectra were obtained for the M7 dwarf vB 8 by Martín (1999) covering a bandpass spanning about 5400–10600 Å. These observations showed the rise and fall of the He I D3 line and the Na I doublet during the flare of this cool dwarf. Crespo-Chacón et al. (2006) obtained medium-resolution optical spectra (3500–7200 Å) for the active M3 star AD Leo to study the chromospheric lines during multiple flares. High-resolution ( $R \sim 60,000$ ) optical spectra (3600–10800 Å) were obtained for the M4 dwarf GJ 699 (Barnard’s star; Paulson et al. 2006), which showed Stark broadening for the Balmer lines. Schmidt et al. (2007) observed a flare for the M7 dwarf 2MASS J1028404–143843 in the red-optical (6000–10000 Å) covering H $\alpha$  and some of the Paschen lines. Fuhrmeister et al. (2008) studied a flare around the M5.5 dwarf CN Leo using observations spanning 3000–10500 Å, at  $R \sim 40,000$ . These observations identified not just a range of chromospheric lines in emission but also continuum enhancement and line asymmetry. Fuhrmeister et al. (2007) obtained simultaneous observations of flaring activity around the M5.5 dwarf CN Leo spanning 3000–10500 Å, at  $R \sim 40,000$ , as well as X-ray data from XMM Newton. Fuhrmeister et al. (2011) observed a flare in the optical at  $R \sim 45,000$  around Proxima Centauri, the closest star to the Sun, which was contemporaneous with observations in the X-ray. Using these measurements, they also discuss theoretical models to constrain the chromospheric properties of the star during the flare. Honda et al. (2018) reported observations of a stellar flare around EV Lac (M4) spanning 6350–6800 Å at  $R \sim 10,000$ , covering H $\alpha$  and the He I lines. They studied the line asymmetries associated with the wings of H $\alpha$  associated with different stages of the flare. Kowalski et al. (2019) reported near-UV (2444–2841 Å) spectroscopic observations of the M4 dwarf GJ 1243, which showed an increase in the broadband continuum during flare events. Recently, Muheki et al. (2020) studied AD Leo at  $R \sim 35,000$  from 4536 to 7592 Å to gain insight into flares and coronal mass ejections.

Guedel & Benz (1993) suggest that the plasma heating and X-ray luminosities from particle accelerations during the quiescent phase should dramatically change around the M7 spectral subtype. Yet the spectral properties of flares around ultracool dwarfs are similar to those around earlier M dwarfs. Lacy et al. (1976; for an updated plot, see Osten et al. 2012) showed that the average flare energy release rate and average flare energy are correlated with the quiescent bolometric luminosity of the star, yet we see flares for ultracool dwarfs that release energy comparable to their bolometric luminosity. The growing suite of instruments (Habitable-zone Planet Finder (HPF), CARMENES, SPIROU, MAROON-X, IRD, NIRPS; Mahadevan et al. 2014; Quirrenbach et al. 2014; Seifahrt et al. 2016; Wildi et al. 2017; Kotani et al. 2018; Donati et al. 2020) searching for planets around M dwarfs using high-resolution Doppler spectrographs in the optical and near-IR (NIR) offers an increasing volume of spectra that is useful for serendipitous stellar flare observations (e.g., Fuhrmeister et al. 2020) to

answer these open questions about flares around ultracool dwarfs.

Not only are M dwarfs the most common spectral type of stars in the Galaxy (Henry et al. 2006), but also they typically host more than one rocky exoplanet (Dressing & Charbonneau 2015; Mulders et al. 2015; Hardegree-Ullman et al. 2019). They present favorable targets for planet detection owing to their smaller radii and masses compared to solar-type stars (Scalo et al. 2007; Irwin et al. 2015) and are also favorable for planetary atmospheric characterization (Batalha et al. 2019). Understanding the occurrence and energetics of flares around M dwarfs is crucial not just from a stellar astrophysics perspective but also to understand the stellar environment influencing the evolution of exoplanets and their atmospheres (Luger et al. 2015; Cuntz & Guinan 2016; Owen & Mohanty 2016; McDonald et al. 2019).

In this work, we present observations and analysis of high-resolution NIR spectra of vB 10, which were obtained with HPF on the 10 m Hobby-Eberly Telescope (HET), where a stellar flare was serendipitously detected. In Section 2, we discuss the target and previous studies associated with its flaring activity. In Section 3, we discuss the observations and processing performed on the spectra. In Section 4, we discuss photometric observations that are almost contemporaneous with the spectra and help us estimate the continuum enhancement during this flare. In Section 5, we detail the analysis performed on the spectral lines seen in the vB 10 flares and place it in the context of other flares seen around similar stars. In Section 6, we estimate the bolometric luminosity of the flare, as well as its frequency. We also discuss the implications of such flares for planetary atmosphere escape, and we conclude in Section 7.

## 2. vB 10

vB 10 (GJ 752 B, 2MASS J19165762+0509021), discovered by van Biesbroeck in 1944 (van Biesbroeck 1944), is a relatively slowly rotating ( $v \sin i \sim 2.7 \text{ km s}^{-1}$ ; Reiners et al. 2018), fully convective M8 star (Liebert et al. 1978; Kirkpatrick et al. 1995) with a  $\log(L_{\text{bol}}/L_{\odot})$  of  $-3.36$  (Tinney et al. 1993).

Flares on very cool M dwarfs have been known since Herbig (1956) first discovered dramatic brightening in Balmer lines and Ca II H and K in vB 10. It also has an extensive history of multiwavelength flare observations: Linsky et al. (1995) observed a flare in UV chromospheric and transition region lines with the Goddard High Resolution Spectrograph on the Hubble Space Telescope (HST). Fleming et al. (2000) first reported an X-ray flare from vB 10, whereas Berger et al. (2008) conducted simultaneous X-ray, UV, and optical observations and observed several flares on vB 10.

## 3. HPF Spectroscopy

HPF (Mahadevan et al. 2012, 2014) is an NIR cross-dispersed echelle spectrograph ( $R \sim 55,000$ ) spanning 8100–12800 Å. It is located at HET, McDonald Observatory, Texas, USA (Ramsey et al. 1998), and is an environmentally stabilized (Stefansson et al. 2016), fiber-fed spectrograph (Kanodia et al. 2018). vB 10 was observed as part of the long-term HPF monitoring and guaranteed time of observation program that began in 2018 April. Each visit included two individual exposures with a total exposure time of

<sup>23</sup> For an introduction to M dwarf flares, refer to Reid & Hawley (2000).

**Table 1**  
Summary of the HPF Observations Analyzed in This Paper

Object	JDUTC <sup>a</sup>	S/N <sup>b</sup>	Exp. Time	Comment
vB 10	2019 Aug 20 05:40	105	945 s	Flare—T1
vB 10	2019 Aug 20 05:57	119	945 s	Flare—T2
vB 10	2018 Sept 24 03:20	132	945 s	Template
vB 10	2018 Sept 24 03:36	144	945 s	Template
HR 3437	2018 Nov 22 11:36	398	330 s	Inst. Response A0
16 Cyg B	2020 Mar 24 11:41	271	202 s x5	Inst. Response G3

**Notes.**

<sup>a</sup> Start of HPF exposure.

<sup>b</sup> Per 1D extracted pixel, calculated as the median S/N for HPF order index 18 ( $\sim 10630\text{--}10770$  Å).

945 s, in sampling-up-the-ramp (SUTR) mode, where each subframe has an integration time of 10.6 s, and all these nondestructive readout (NDR) frames are combined to calculate a single 2D flux image on the detector. This allows us to reconstruct the change in the measured spectra as a function of time.

As part of these observations,<sup>24</sup> spectra were obtained for vB 10 during a flare on 2019 August 20 (JDUTC  $\sim 2,458,715.75$ ) for  $2 \times 945$  s exposures starting at 05:40 UTC. These observations are summarized in Table 1.

We use the algorithms from `HxRGPROC` (Ninan et al. 2018) for bias noise removal, nonlinearity correction, cosmic-ray correction, and slope/flux and variance image calculation of the raw HPF data. This variance estimate is used to calculate the signal-to-noise ratio (S/N) of each HPF exposure (Table 1). In addition, we flat-correct the data and extract them following the procedures in Ninan et al. (2018) and Metcalf et al. (2019). After extracting the 2D spectrum to a 1D flux versus wavelength grid, we correct for telluric absorption, as well as emission lines, and then shift the spectrum to the stellar rest frame. We then flux-calibrate the spectrum and correct for the chromatic instrument response. Finally, we subtract a quiescent phase spectrum from the flare spectrum to quantify the emission during the flare. The procedure for this is detailed in Appendix A. All HPF spectra shown and discussed in this paper are in vacuum wavelengths.

#### 4. HET Acquisition Camera (ACAM) Photometry

As part of the target acquisition at HET, vB 10 was observed on the HET acquisition camera (ACAM), which has a field of view of  $3'5 \times 3'5$ . Typical HPF acquisition includes a few ACAM images before the HPF exposures to locate the target and then move it to the HPF telescope fiber (Kanodia et al. 2018), as well as one ACAM image after the HPF exposure. The images were taken using the Sloan Digital Sky Survey (SDSS)  $i'$  filter,<sup>25</sup> with exposure times varying between 3 and 10 s, and  $1 \times 1$  on-chip binning. We use these ACAM images to perform differential aperture photometry on vB 10 and search for any enhancement in the broadband continuum during the flare. The procedure followed to reduce the photometry is detailed in Appendix B.

We show the photometry from the HET ACAM in Figure 1. An ACAM sequence of exposures spanning  $\sim 3$  minutes was

taken preceding T1, which ended under 1 minute before the start of the HPF exposure (Flare—T1; Table 1). Additionally, one ACAM exposure was taken about 1 minute after the end of the HPF exposure (Flare—T2). We note that the fluxes during this sequence of exposures before T1 are  $\sim 12\%$  higher than the median normalized baseline over the entire observing sequence. The implications of this continuum enhancement are discussed in Section 6.2.

#### 5. Results for Activity-sensitive Features

In this section we discuss the fluxes measured from the subtracted spectrum of the activity-sensitive features during the stellar flare observed in vB 10 with HPF. Optimized to obtain precise radial velocities (RVs) on mid- to late M dwarfs, the HPF bandpass covers the Ca II infrared triplet (IRT), as well as the He I  $\lambda 10830$  transitions. Additionally, it spans the wavelength range of Pa $\gamma$  (Pa 6) through the Paschen jump. That said, most of the Paschen lines are either contaminated by water vapor or, in the case of the higher Paschen transitions, not seen. We also see several atomic lines in emission during the flare.

All the spectra discussed hereafter are telluric corrected (Section A.1), shifted to the stellar rest frame (Section A.2), response corrected (Section A.3), flux-calibrated (Section A.4), and quiescent phase subtracted (Section A.5). This enables us to measure the energy emitted in these spectral features during the flare. In Table 2, we list the lines we analyzed, as well as the measured fluxes for these lines during the two HPF observations. The fluxes are measured by performing a Gaussian fit to calcium, iron, and magnesium lines and a Lorentzian fit to the Paschen and helium lines. We propagate the error from the raw spectra and calculate a final statistical error for the line fluxes to be  $\sim 1\%$ , which is consistent with the S/N of the observed spectra  $\sim 100$  (per 1D extracted pixel, calculated as the median S/N for HPF order index 18 ( $\sim 10630\text{--}10770$  Å); Table 1). However, to be conservative, we also ascribe a systematic error of 15% to the flux estimates based on the response correction (Section A.3). We also compare the central wavelength from the line fit to the rest wavelength (Kramida 2010) and find the fits to be consistent with zero velocity offsets, with an absolute upper limit equivalent to the instrument resolution at  $\sim 5$  km s<sup>-1</sup>. This indicates the absence of bulk flowing material during the flare. This is consistent with the interpretation that these observations are during the decay phase of the flare (Section 5.1). Unlike Fuhrmeister et al. (2008), Fuhrmeister et al. (2011), and Honda et al. (2018), we do not find any asymmetries in the Ca lines, while noting a weak red asymmetry excess for the Pa 6 ( $\gamma$ ) line. Additionally, we discuss a red asymmetry seen in the He triplet in Section 5.3. In addition, we also reconstruct the temporal evolution of the fluxes across each 945 s exposure by using the SUTR subframes across 3 intervals of 315 s each.

There are very few reported observations to date of flares on ultracool M dwarfs at high spectral resolution, and even fewer that include the NIR HPF bandpass. Schmidt et al. (2012) report on some of the first NIR observations using TripleSpec at the ARC 3.5 m telescope, but they have very limited overlap with HPF and report no IR data on vB 8, their latest spectral type target. The closest comparison to our vB 10 spectrum comes from flare observations reported by Liebert et al. (1999) for 2MASSW J0149090+295613 (an M9.5 dwarf, hereafter referred to as 2M0149), as well as from Schmidt et al. (2007)

<sup>24</sup> Observations from 2018 April to 2020 October were analyzed for this work.

<sup>25</sup> Centered at 7718 Å with an FWHM of 1564 Å.

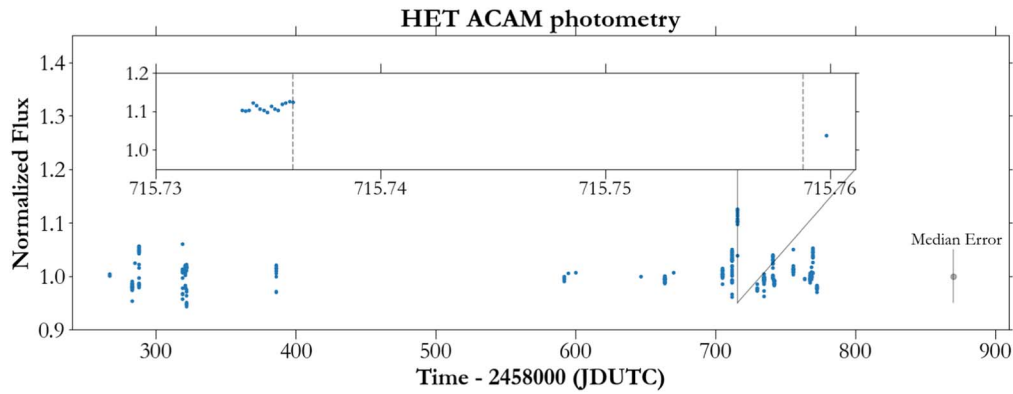


**Figure 1.** Relative photometry of  $\nu$ B 10 as seen by HET ACAM, with a typical error of  $\sim 5\%$  on each point. The inset shows the acquisition photometry preceding T1, with the span of the HPF observations marked with the dashed lines. We see a 12% enhancement in the photometry preceding the HPF observing window (marked with the dashed lines), while our median error of  $\sim 5\%$  is also plotted for representative purposes. Since the photometry is consistently elevated across 15 ACAM exposures to  $\sim 12\%$  before T1, we do not attribute this enhancement to a statistical anomaly, and we discuss the implications in Section 6.2.

**Table 2**

List of the Lines in Emission That Are Analyzed, with the Fluxes Measured as Described in Section 5, with a Typical Uncertainty on the Fluxes of  $\sim 15\%$

Atomic	HPF Order	Wavelength		Line Integral Flux		Luminosity	
		( $\text{\AA}$ )		$(\times 10^{-14} \text{ erg s}^{-1} \text{ cm}^{-2})$		$(\times 10^{25} \text{ erg s}^{-1})$	
Line	Index <sup>a</sup>	Vacuum	Air	T1	T2	T1	T2
Ca II	3	8500.4	8498	3.01	2.08	12.04	8.32
Ca II	4	8544.4	8542.1	3.02	2.27	12.08	9.08
Ca II	5	8664.5	8662.1	2.31	1.87	9.24	7.48
Fe I	5	8691	8688.6	0.208	0.152	0.83	0.61
Pa 12 <sup>b</sup>	5	8752.9	8750.3	0.296	0.224	1.18	0.90
Mg I	6	8809.2	8806.8	0.215	0.248	0.86	0.99
Fe I	6	8826.6	8824.2	0.214	0.213	0.86	0.85
Pa 11 <sup>b</sup>	6	8865.2	8862.9	0.524	0.402	2.10	1.61
Pa 7 ( $\delta$ ) <sup>b</sup>	14	10052.1	10049.4	1.48	0.999	5.92	4.00
He I <sup>b</sup>	19	10832.1	10829.1	1.28	1.1	5.12	4.4
He I <sup>b</sup>	19	10833.2	10830.2	1.54	1.42	6.16	5.68
He I <sup>b</sup>	19	10833.3	10830.3	1.54	1.42	6.16	5.68
Pa 6 ( $\gamma$ ) <sup>b</sup>	19	10941.1	10938.1	1.75	1.08	7.00	4.32

**Notes.** All wavelengths listed below are in the stellar rest frame in vacuum and corrected to the stellar rest frame (Kramida 2010). A machine-readable version of this table is included with this paper.

<sup>a</sup> Zero indexed HPF orders.

<sup>b</sup> Lorentzian fit.

(This table is available in machine-readable form.)

for 2MASS J1028404–143843 (an M7 dwarf, hereafter referred to as 2M1028). We contrast our HPF  $\nu$ B 10 observations with these two data sets that span a bandpass from blueward of  $H\alpha$  to about  $1 \mu\text{m}$ , albeit at a much lower spectral resolution. In addition, they also bracket  $\nu$ B 10 (M8) in spectral type.

### 5.1. Ca Infrared Triplet

The Ca II IRT lines are a relatively well studied activity indicator in M dwarfs and other stars with solar-like magnetic activity. Martin et al. (2017) measure the flux excess for a number of G and K stars after subtracting the spectrum of an inactive template star. They demonstrate that the IRT is well correlated with the traditional activity indicators based on Ca II H and K lines, such as  $R'_{\text{HK}}$  and  $S_{\text{MWO}}$ . Based on optical spectra for the M5.5 dwarf Proxima Centauri, Robertson et al. (2016) show a correlation between the IRT and  $H\alpha$ . Schöfer et al. (2019) also use the spectral subtraction methods with the extensive CARMENES (Quirrenbach et al. 2014) M dwarf data set to study the correlation between the IRT and other lines.

The IRT is the strongest activity indicator in the HPF bandpass. The quiescent-subtracted spectrum for the IRT is shown in Figure 2.

We also compare the flux emitted in the IRT in  $\nu$ B 10 with 2M0149 and 2M1028 for the strongest line  $\lambda 8544.4$ . Normalized for distance (Table 3), the flux in 2M1028 appears to be  $54\times$  stronger, and the emission seen in 2M0149 is about  $2\times$  stronger. The ratio of the IRT lines, and particularly of  $\lambda 8544.4$ , the strongest, to  $\lambda 8500.4$ , the weakest, is a useful indicator of stellar activity. This ratio is typically 9.1 in solar prominences (Landman & Illing 1977) and 1.7 in a solar flare observed with the Lick Hamilton Echelle (Johns-Krull et al. 1997). In active binaries, the ratio of residual emission in the  $\lambda 8544$  line to the  $\lambda 8500$  line is typically 1.2–1.6 (Hall & Ramsey 1992; Montes et al. 2000).

The flare observations yield a line ratio for  $\lambda 8544/\lambda 8500 \sim 1$  for the first observation, which increases to 1.1 for the second. This indicates that the flare was optically thick during this phase, while softening. This is further corroborated by the

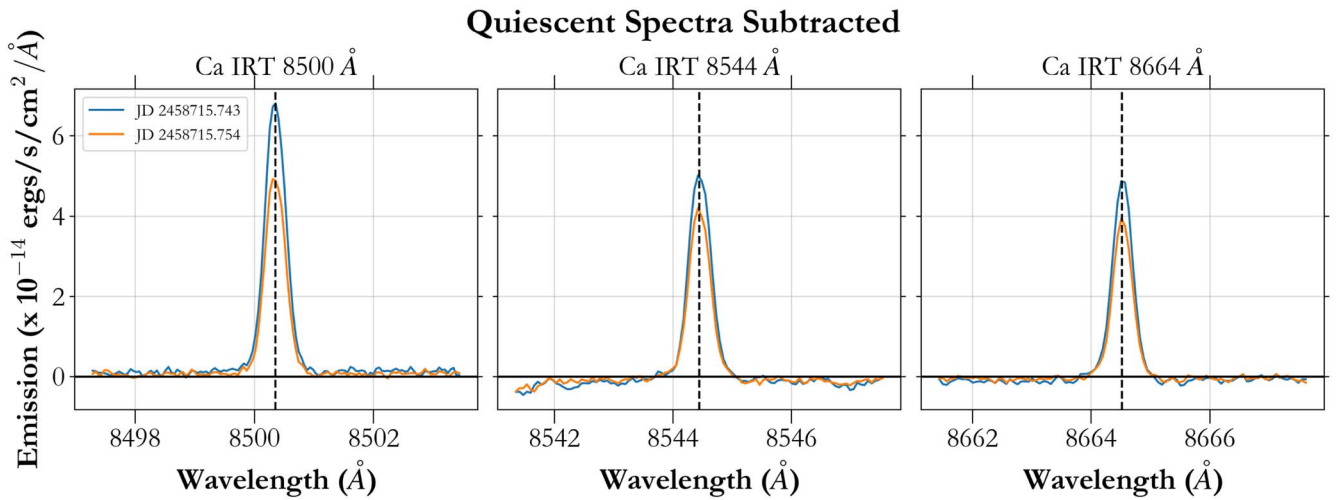


**Figure 2.** Quiescent-subtracted spectrum from HPF showing the emission in the Ca IRT seen in vB 10. The dashed lines mark the rest position of each line. The two different colors indicate the successive HPF observations.

**Table 3**  
Gaia EDR3 Parallax Measurements (Collaboration et al. 2021)

Name	Gaia EDR3 ID	Parallax (mas)	Distance (pc)
vB 10	4293315765165489536	168.9	5.92
2M0149	302525062400087936	42.4	23.6
2M1028	3752240939122060160	28.9	34.6

decreasing fluxes as discussed in Section 5.6. The ratio of the other IRT lines  $\lambda 8544/\lambda 8665$  is  $\sim 1.3$  for the first observation and 1.2 for the second observation. We note that it is unphysical for the ratio of  $\lambda 8544/\lambda 8500$  to be less than the  $\lambda 8544/\lambda 8665$  ratio;<sup>26</sup> however, these ratios are consistent given the flux uncertainty of  $\sim 15\%$  detailed in Section A.3, especially in order 3 with the instrument response asymmetry.

For 2M1028, the ratios of  $\lambda 8544/\lambda 8500$  and  $\lambda 8544/\lambda 8665$  are  $\sim 1.36$  and  $\sim 1.34$ , respectively. Similarly, for 2M0149, the ratios are  $\sim 1.48$  and  $\sim 1.32$ , respectively. It is clear from the IRT fluxes that the material creating the excess emission in vB 10 is optically thick, and the decaying nature (in both strength and optical thickness<sup>27</sup>) supports that it is a flare event.

### 5.2. Paschen Lines

There are several Paschen lines that fall within the HPF bandpass, of which Pa 12, Pa 11, Pa 7 ( $\delta$ ), and Pa 6 ( $\gamma$ )<sup>28</sup> are measured to be in emission during the flare without significant telluric contamination (Table 2). The aforementioned studies for 2M1028 and 2M0149, as for the IRT, remain the best comparisons. Observations of Paschen emission in a solar white-light flare from 1981 April are discussed by Neidig & Wiborg (1984) and are in the context of detecting the Paschen continuum. Figure 3 shows the HPF vB 10 quiescent-

<sup>26</sup> According to Landman & Illing (1977), the ratio of intensities for the IRT when optically thin should be  $1/9 : 1 : 1/2$ , respectively. Therefore, the  $\lambda 8662$  line should be  $4-5 \times$  stronger than the  $\lambda 8500$  line when optically thin; conversely, under optically thick conditions they should be of similar intensities.

<sup>27</sup> As the material that is creating the excess emission reduces in density with time, the line ratios increase, thereby tending toward being optically thin; simultaneously, the line fluxes are also diminishing as shown in Figure 9.

<sup>28</sup> Pa 5 ( $\beta$ ) falls just redward of the HPF bandpass.

subtracted spectrum for these Pa lines during the flare. We note the broad wings present in the Paschen lines, which resemble the broad Balmer lines observed in a flare around GJ 699 by Paulson et al. (2006), which is indicative of linear Stark broadening (Paulson et al. 2006).

The temporal decay for the Pa 6 line is discussed in Section 5.6. We also look at the relative decrement in the Paschen lines, plotting the normalized fluxes of the lines versus the quantum number of the upper level of the Paschen transition (Figure 4). We choose to normalize with respect to Pa 7 ( $\delta$ ) in this case because it is the lowest level that is common to vB 10 and 2M0149. The overlap in Paschen lines between the 2M1028 flare and the flare discussed here is too small and is not included here. We note that Pa 6 ( $\gamma$ ) in vB 10 lies below the reference line (Figure 4), showing evidence of saturation.

### 5.3. He I Triplet

The He  $\lambda 10830$  triplet is one of the strongest emission features we see in the flare spectrum (Figure 5). We note that the ratio of T2/T1 for the triplet is similar to the other emission lines we observe (Figure 9). We note that unlike the gradual He I line decay reported by Schmidt et al. (2012) for a flare around EV Lac (Figure 4), our data indicate a relatively rapid decay in the He fluxes. The two red triplet lines at  $10833.2 \text{ \AA}$  (vacuum; air =  $10830.3 \text{ \AA}$ ) are blended, while the weaker bluer line is clearly distinguished (Figure 7). In the optically thin regime, the ratio of  $I_{\text{blue}}/I_{\text{red}}$  is  $\sim 0.12$ .<sup>29</sup> We perform a three-component Voigt fit to the He I emission using astropy (Astropy Collaboration et al. 2018); in addition, the model includes a Gaussian component to fit the red excess discussed in the next section. With the two red components of the triplet separated by just  $0.1 \text{ \AA}$ , there exists a degeneracy in the estimation of their widths and amplitudes. We obtained the best fit to the helium excess when the two red components were bound to have the same amplitude and widths. Comparing the integrated area under each line, we obtain a ratio for  $I_{\text{blue}}/I_{\text{red}}$  of  $\sim 0.35$ , which is consistent with being optically thick.

<sup>29</sup> The line strengths are proportional to the product of the Einstein coefficient  $A_{ji}$  and the degeneracy  $g_j$ . Therefore,  $I_{\text{blue}}/I_{\text{red}} \sim (A_{\text{blue}} \cdot g_{\text{blue}}) / (A_{\text{red1}} \cdot g_{\text{red1}} + A_{\text{red1}} \cdot g_{\text{red2}}) \sim 0.12$  (Kramida et al. 2020).

### Quiescent Spectra Subtracted

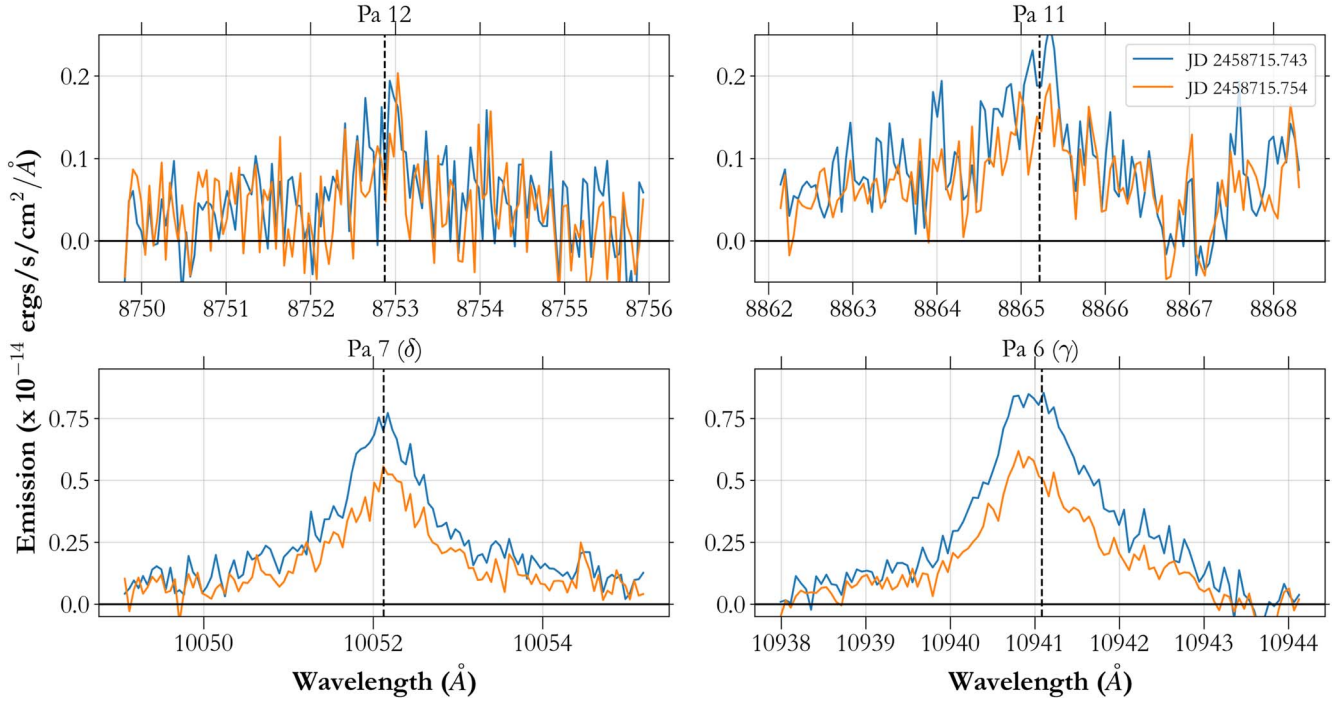


**Figure 3.** Quiescent-subtracted spectrum from HPF showing the Pa lines seen in emission in vB 10. The dashed lines mark the rest position of each line. Blue and orange depict the two observations—T1 and T2, respectively.

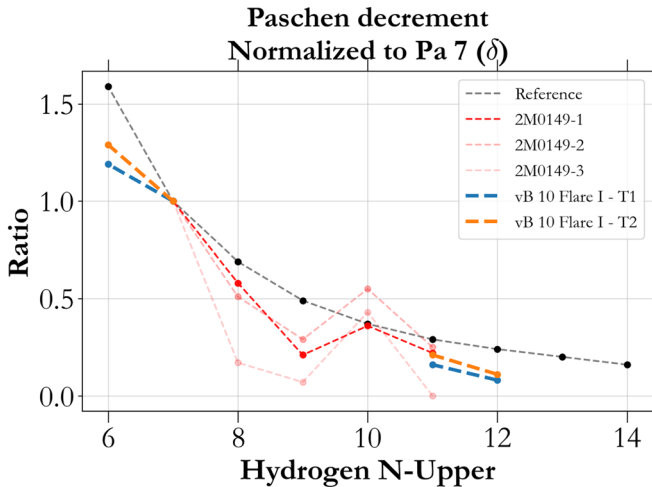


**Figure 4.** The relative decrement of the vB 10 spectrum (blue and orange), compared to the 2M0149 observations (red). The reference line (black) is the Pa line decrement (Osterbrock 1989) normalized to Pa 7.

Fuhrmeister et al. (2019) and Fuhrmeister et al. (2020) report on the extensive He  $\lambda 10830$  data set from the CARMENES survey, where the average of vB 10 observations is reported. In the 2020 paper, they explore the He  $\lambda 10830$  variability and discuss some cases of flaring, but not specifically for ultracool dwarfs.

#### 5.4. Other Lines Seen in Emission

In addition to the more familiar activity-sensitive features discussed above, we also observe other atomic features listed in Table 1, which we could reliably measure fluxes for (Figure 6). The two Fe I multiplet lines at 8691 and 8826 Å were also

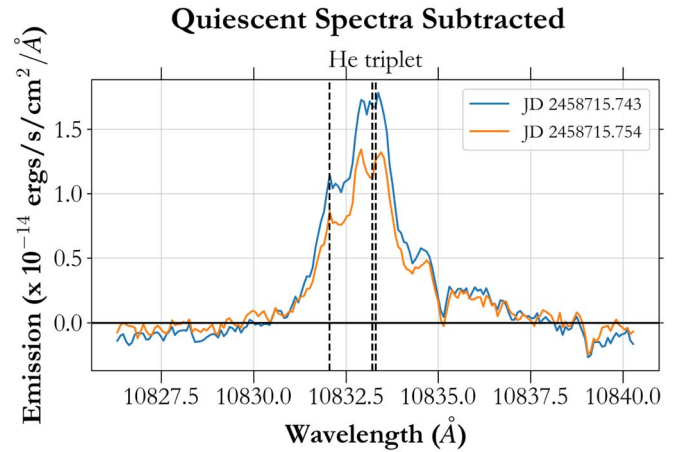


**Figure 5.** Quiescent-subtracted spectrum from HPF showing the He triplet lines seen in emission in vB 10. The dashed lines mark the rest position of each line. The two different colors indicate the successive HPF observations. The triplet is one of the strongest emission features we see in the HPF spectra and is consistent with being optically thick.

observed by Fuhrmeister et al. (2008) in CN Leo and were  $\sim 10 \times$  stronger. The Mg I line at 8809 Å was also observed to be  $\sim 30 \times$  stronger in the CN Leo flare. The strength difference between the two flares is not surprising, since the CN Leo observations were close to the flare peak, and as mentioned before, the vB 10 data are in the decay phase of the flare.

#### 5.5. Red Asymmetry

We note the excess emission in the red wing of the He I triplet at  $\sim 10836$  Å (Figure 7), which can be attributed to downward mass motion, due to either chromospheric condensation (Ichimoto & Kurokawa 1984; Canfield et al. 1990;

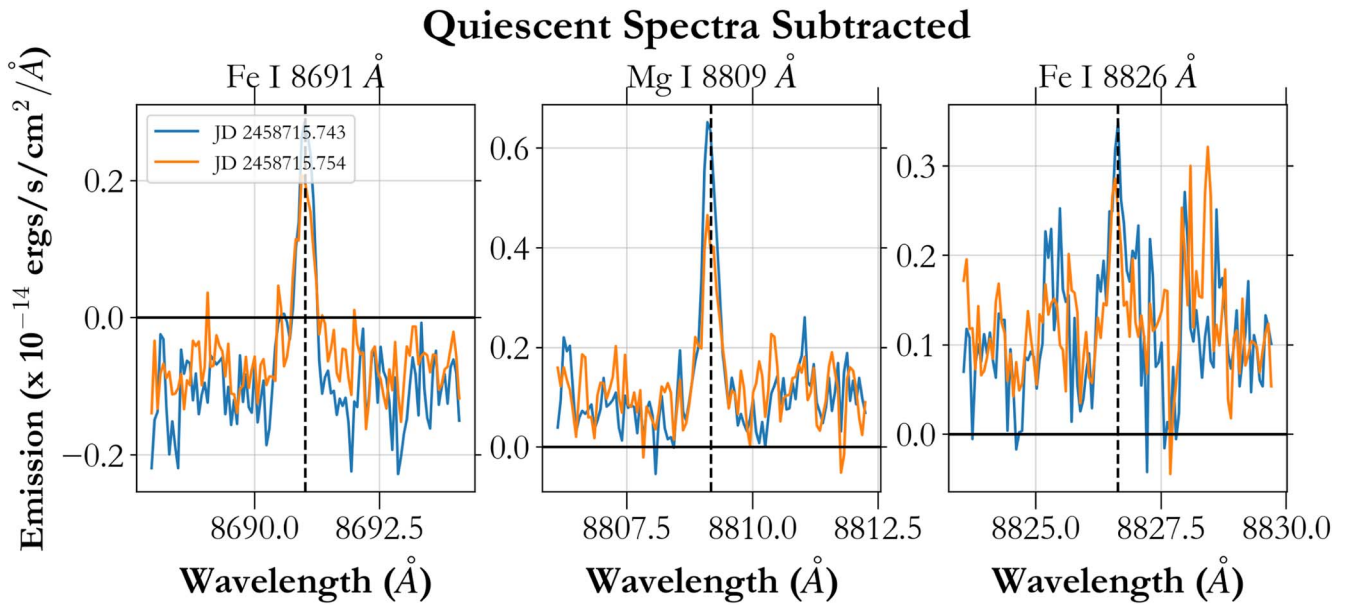


**Figure 6.** Quiescent-subtracted spectrum from HPF showing the metal lines seen in emission in vB 10. The dashed lines mark the rest position of each line. The blue and orange lines indicate T1 and T2, respectively.

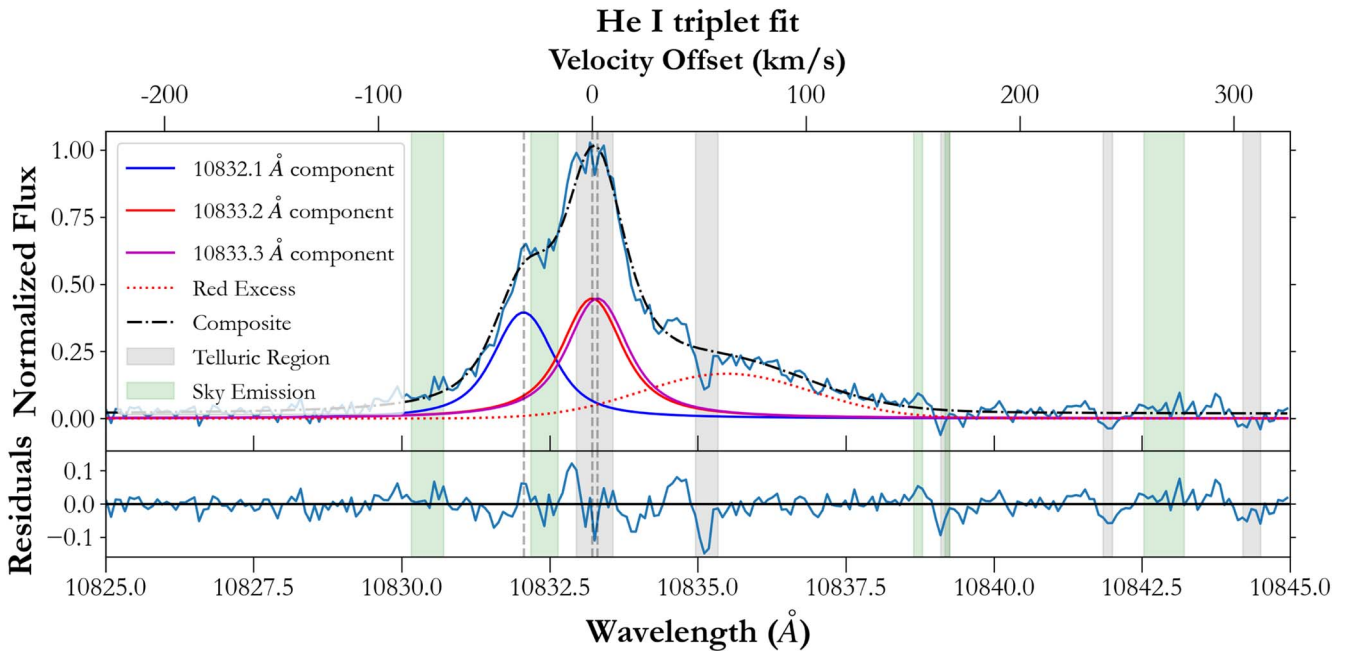


**Figure 7.** Voigt fit to the He triplet emission for T1 (Figure 5), showing the three components, as well as excess emission at the red wing of the triplet ( $\sim 10836 \text{ \AA}$ ). The rest wavelength for each line is marked with a dashed line. The shaded gray regions indicate where the telluric model (Section A.1) shows  $>10\%$  telluric absorption (before correction) and are masked while fitting the line profiles. Similarly, the green regions mark the sky emission lines. We also fit the red excess with a Gaussian and find the peak of the red components at about ( $10835.5 \text{ \AA}$ ). The red excess seen here is about 30% in magnitude of the total He I triplet emission.

Graham & Cauzzi 2015; Graham et al. 2020) or coronal rain (Antolin & Rouppe van der Voort 2012; Judge et al. 2015; Lacatus et al. 2017; Ruan et al. 2021) depending on the temporal morphology of the emission. Coronal rain is typically seen in the gradual phase of the flare (similar to our T1–T2 observations). Conversely, chromospheric condensation is generally observed in the impulsive phase, even though there have been solar observations that show that this is not always the case (Graham et al. 2020). Given that we do not see a similar asymmetry in the Ca IRT, we infer this emission to be originating from the upper chromosphere or corona.

We fit the red excess with a Gaussian and estimate the velocity offset for this feature (to the primary lines) to be  $\sim 70 \text{ km s}^{-1}$  (Figure 7), which is consistent with the average of  $60\text{--}70 \text{ km s}^{-1}$  measured by Antolin & Rouppe van der Voort (2012) and Lacatus et al. (2017) and  $\sim 100 \text{ km s}^{-1}$  by Fuhrmeister et al. (2018). Using this fit, we estimate the standard deviation of the Gaussian to be  $1.4 \text{ \AA}$  (corresponding to a  $kT$  temperature of 22,000 K) and the flux emitted in this red excess to be  $\sim 30\%$  of the He I triplet. We also perform a similar analysis for the second HPF visit on this flare, T2, and obtain a similar velocity offset, width, and flux ratio. We do not

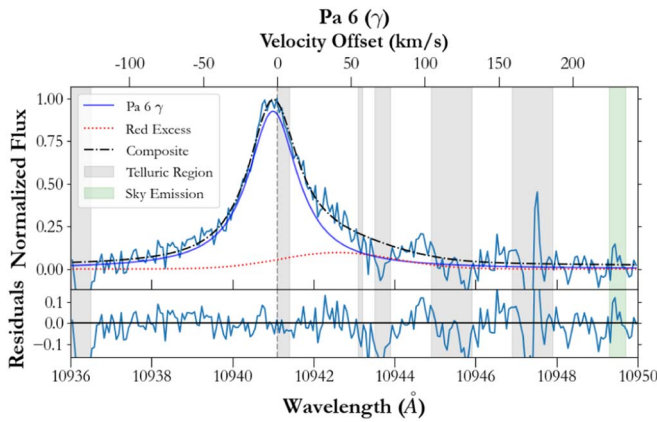


**Figure 8.** Similar to the fit for the He I triplet, we fit a Voigt profile to the Pa 6 ( $\gamma$ ) line and note a very weak excess over the red wing of the Pa line. The rest velocity for the Pa line is marked by the dashed line. The shaded gray regions indicate regions where the telluric model (Section A.1) shows  $>10\%$  telluric absorption (before correction) and is masked during line fitting, whereas the green regions mark the sky emission lines. Note that the wavelength limits in this plot are larger than Figure 3, to illustrate the wings of the line.

measure an appreciable evolution in the velocity of this asymmetry in the higher time resolution (albeit lower-S/N) SUTR time series, which is also consistent with the coronal rain hypothesis (Graham et al. 2020). This also agrees with solar coronal rain measurements in post-flare loops, which follow 40–80 minutes after the impulsive phase in the form of sudden condensation events (Figures 1 and 2; Ruan et al. 2021). Simulations for the Sun indicate the occurrence of quasi-periodic pulsations in plasma after such coronal rain events (Ruan et al. 2021), which have been observed around M dwarfs, most recently using photometry (Ramsay et al. 2021) from the Transiting Exoplanet Survey Satellite (TESS; Ricker et al. 2014).

We also note a possible weak excess redward ( $\sim 50$ – $150$   $\text{km s}^{-1}$ ) of Pa 6 ( $\gamma$ ) (Figure 8) that is not detected for the other Pa lines. While further inference is impeded by artifacts from telluric correction, we fit a Gaussian of width similar to that of the He triplet (1.4  $\text{\AA}$ ) to this asymmetry in the Pa line and note a velocity offset of  $\sim 50$   $\text{km s}^{-1}$ , with the flux emitted in the red excess to be  $\sim 15\%$  that of the Pa line.

### 5.6. Temporal Evolution of Atomic Lines

These observations span the gradual decay phase when the lines are reducing in strength. Figure 9 shows the decay for the Ca IRT, an iron line, the He triplet, and the Pa 6 line and can be compared to Figure 4 from Schmidt et al. (2012). In particular, we note that while the He triplet fluxes decay more slowly than the other lines in their flare spectra of EV Lac, our analysis for vB 10 shows that this is not always true, with Figure 9 showing that all the lines analyzed here have similar rates of decay.

## 6. Discussion

### 6.1. Estimating $H\alpha$ Fluxes

#### 6.1.1. Using the Ca II IRT to Estimate $H\alpha$

The  $H\alpha$  transition is one of the most common diagnostics for flares in M dwarfs.<sup>30</sup> The literature on flare spectra in M dwarfs

<sup>30</sup> For M dwarfs, measurements of the Ca II H and K lines are limited by the faintness of the nearby pseudocontinuum.

is extensive but heavily weighted toward earlier spectral subtypes and visible wavelengths. While for the ultracool M dwarfs, it is even more sparse—Berger et al. (2008) summarize extensive optical data in the region 3840–6680  $\text{\AA}$  at  $\sim 5.5$   $\text{\AA}$  spectral resolution, as part of a multiwavelength study of activity in very cool M dwarfs. The 2M1028 and 2M0149 flare observations are unique for late M dwarfs because they both have Ca II IRT and  $H\alpha$  data simultaneously during a flare event. Since the HPF bandpass does not include  $H\alpha$ , we use these observations to obtain a relation between  $H\alpha$  and IRT fluxes for similar stars during flares, and by doing so, we seek to compare the HPF observations of the vB 10 flare with other similar events.

We do not use the  $L_{\text{line}}/L_{\text{bol}}$  values reported with these flare observations, since the luminosity estimates are based on obsolete parallax measurements. We instead use Gaia EDR3 parallax measurements (Table 3) for these three targets (vB 10, 2M1028, and 2M0149).

To get a scaling of  $F_{\text{IRT}}$  to  $F_{H\alpha}$  for 2M0149, we take the ratio of  $H\alpha$  fluxes to the sum of the three IRT fluxes. The average of these scaling factors for the four observations from Table 1 of Liebert et al. (1999) is 6.68. Following the same procedure for 2M1028 yields a factor of 6.64. We use an average of the scaling factor from 2M0149 and 2M1028, i.e., 6.66.

To estimate the  $H\alpha$  flux, we add the three IRT fluxes for T1 to obtain a total of  $8.34 \times 10^{-14}$   $\text{erg s}^{-1} \text{cm}^{-2}$ ; multiplying this by 6.66 gives a vB 10  $H\alpha$  estimate of  $56 \times 10^{-14}$   $\text{erg s}^{-1} \text{cm}^{-2}$ . The T2 fluxes are about 75% of the first spectrum. These extrapolated  $H\alpha$  fluxes are comparable to the fourth and weakest observation reported by Liebert et al. (1999) for 2M0149, and about 2% of the values reported by Schmidt et al. (2007) for 2M1028. Conversely,  $H\alpha$  fluxes reported by Berger et al. (2008) are about 3–4  $\times$  weaker than our estimates for vB 10.

#### 6.1.2. Using the Pa Lines to Estimate $H\alpha$

We also use the Paschen lines to estimate the  $H\alpha$  flux for vB 10. We continuum-subtract the 2M0149 spectrum (Liebert et al. 1999, Table 1) and average the ratio of  $H\alpha$  to Pa 7 ( $\delta$ ) across their four observations to obtain a ratio of 19. Multiplying this ratio (of 19) with the Pa 7 ( $\delta$ ) flux from Table 2—T1, gives the  $H\alpha$  flux to be  $25 \times 10^{-14}$   $\text{erg s}^{-1} \text{cm}^{-2}$ , which is  $\sim 2 \times$  lower than that obtained from the IRT analysis.

### 6.2. Energy Released during the Flare

We follow a procedure similar to Gizis et al. (2017), to estimate the bolometric energy released during the decay phase of this flare from the HET ACAM photometry. We use the BT-Settl model spectrum (Allard et al. 2012) at 2700 K (vB 10  $T_{\text{eff}} = 2745$  K; Fouqué et al. 2018), which is scaled to the Two Micron All Sky Survey (2MASS; Cutri et al. 2003)  $J$  mag = 9.9 (Section A.4). To simulate the flare spectra, we use a blackbody at 10,000 K (Kowalski et al. 2015), generated with *astropy* (Robitaille et al. 2013; Astropy Collaboration et al. 2018).<sup>31</sup> This is then scaled to match the continuum enhancement of  $\sim 12\%$  seen in SDSS  $i'$  using the HET ACAM

<sup>31</sup> We note that the 10,000 K blackbody used is a simplified model. Kowalski et al. (2013) have shown continuum enhancements consistent with blackbody temperatures ranging from 9000 to 14,000 K for a sample of mid-type M dwarf flares, while Gizis et al. (2013) observe a flare around an L1 dwarf and report a white-light flare continuum that corresponds to a 8000 K blackbody.

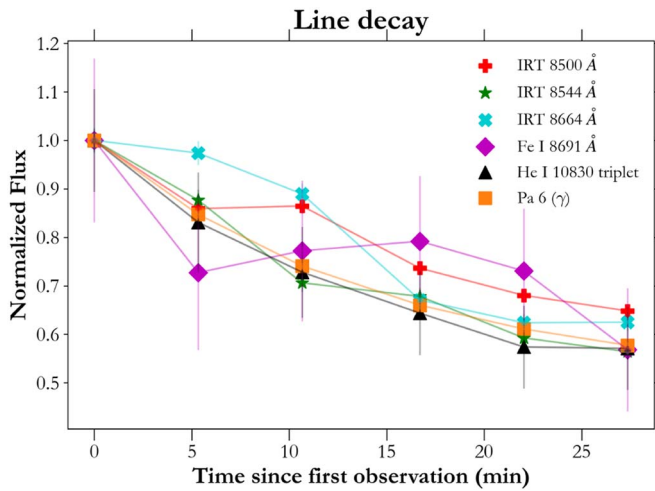


**Figure 9.** We split the 945 s HPF NDR exposure into three subexposures of 315 s each. For each of the lines, we show the normalized fluxes for the six HPF exposures as a function of exposure midpoint. We fit a linear decay to the 315 s fluxes, the average slope of which is about  $-1.5\%$  minute $^{-1}$ . The fluxes for the NDR exposures are calculated by summing across a 2 Å window for the calcium and iron lines and a 5 Å window for the Paschen lines and helium triplet. The window is narrow enough that the relative change in the instrument response across that window is negligible, and hence the error bars depicted in this plot are based on the propagated variance for each line.

photometry before T1 (Section 4). These spectra are plotted in Figure 10; using these, we find the bolometric luminosity during this phase to be  $1.22 \times 10^{29}$  erg s $^{-1}$ , which is about 7% of the bolometric luminosity of the  $\nu$ B 10.

We refer to the analysis of K2 light curves for flares around ultracool dwarfs by Paudel et al. (2018) to approximate the total energy released during this flare. They analyze the temporal morphology of white-light flares around 2M0835+1029 (an M7 dwarf) and 2M1232-0951 (an L0 dwarf), as observed by K2 in the Kepler bandpass.<sup>32</sup> We compare the rate of decay in the IRT fluxes (Section 5.6)<sup>33</sup> with the K2 flare light curve for 2MASS J08352366+1029318 and 2MASS J12321827-0951502. These two flares reach a comparable slope when the fluxes reach 12% and 8% of the peak flux, respectively. Taking the average of these two, we estimate that our measurements of the bolometric luminosity using the HET ACAM photometry are at about 10% of the peak emission of  $10 \times 1.22 \times 10^{29}$  erg s $^{-1}$ , or  $\sim 1.22 \times 10^{30}$  erg s $^{-1}$ . This is  $\sim 70\%$  of the total bolometric luminosity of the star. Furthermore, we integrate the area under the two K2 flare curves and obtain the total energy released during the flares to be  $\sim 8.5 \times$  the peak energy, i.e., for the  $\nu$ B 10 flare, the total energy should approximate  $\sim 10^{31}$  erg. We note that this estimate is approximate, with an error of 50%–100% because of the assumptions made regarding the temporal morphology of these flares, as well as the error present in the flux estimates from the HET photometry. Since we do not have observations spanning the entirety—both temporally and in wavelength—of the flare, we use these comparisons to understand the nature of the flare.

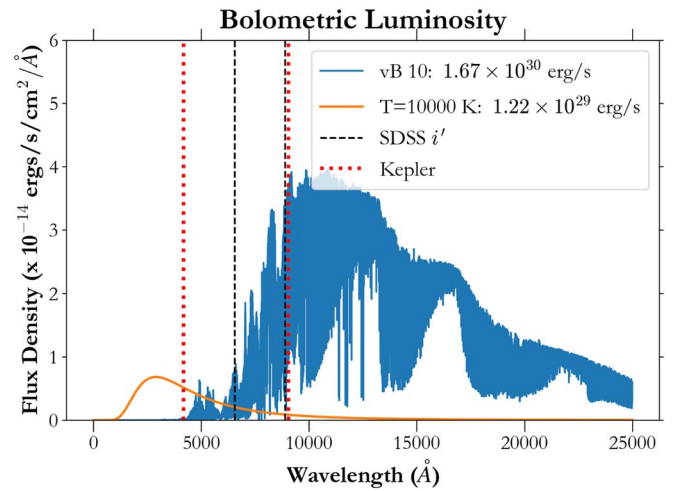


**Figure 10.** In this plot we show a BT-Settl model spectrum (Allard et al. 2012) at 2700 K for  $\nu$ B 10, in addition to a scaled 10,000 K blackbody. The black dashed line indicates the SDSS  $i'$  bandpass used for the observations in Section 4 to estimate the continuum enhancement, while the red dotted line shows the Kepler bandpass used for the analysis in Section 6.3. The bolometric luminosity for  $\nu$ B 10 is  $1.67 \times 10^{30}$  erg s $^{-1}$  (Tinney et al. 1993), while that for the 10,000 K blackbody is  $1.22 \times 10^{29}$  erg s $^{-1}$ . This suggests that right before the HPF observations the bolometric luminosity of the flare was  $\sim 7\%$  of the total luminosity of the star.

### 6.3. Estimating the Flare Frequency

Paudel et al. (2018) average the flare rates for ultracool dwarfs across different spectral types, as a function of the total energy released in the Kepler bandpass during the flare. To estimate the flare frequency using these, we need to calculate the energy released for  $\nu$ B 10. To do so, we multiply a blackbody of 10,000 K (Section 6.2) by the Kepler bandpass (Figure 10) and integrate it to estimate a luminosity during the decay phase in the Kepler band of  $2.5 \times 10^{28}$  erg s $^{-1}$ . Based on the scaling obtained in the previous section, this corresponds to  $2 \times 10^{30}$  erg released in the Kepler bandpass during the flare. In Figures 10 and 12(a) from Paudel et al. (2018), this flare energy corresponds to an average flare frequency of once every 100 or 120 hr, respectively.

We also use HPF observations to place an independent upper limit on the cadence of flares of similar energy on  $\nu$ B 10. We attempted to bound the flare rate of  $\nu$ B 10 under the assumption that—as shown for other M dwarfs (e.g., Pettersen & Hawley 1989; Chang et al. 2015; Li et al. 2018)—the star flares at times well described by a Poisson distribution. With only one flare in the data set, we are unable to fully constrain the flaring frequency of  $\nu$ B 10 for such flares, but we can provide an upper bound.

We created simulated time series of flares, representing the flare series as a square wave with Poisson-distributed pulses. The height of each pulse is constant, as we seek to constrain the frequency of any flares energetic enough to be clearly noticed in the HPF spectral series. The temporal spacing of the simulated flares is determined by a wait time (the average time between flare events), and the number of flares per flare series is set such that the time baseline of the series matches or exceeds the baseline of the HPF data. We run this simulation for a flare duration (=pulse width) of 1 hr.

For each flare wait time, 10,000 trials are performed, with each trial creating a new flare series and new flare distribution. For each trial, we consider an individual simulated flare to be

<sup>32</sup> Spanning 4183–9050 Å with an FWHM of 3993 Å.

<sup>33</sup> This is consistent with the slope to a linear fit to the Pa 6 ( $\gamma$ ) flux decay.

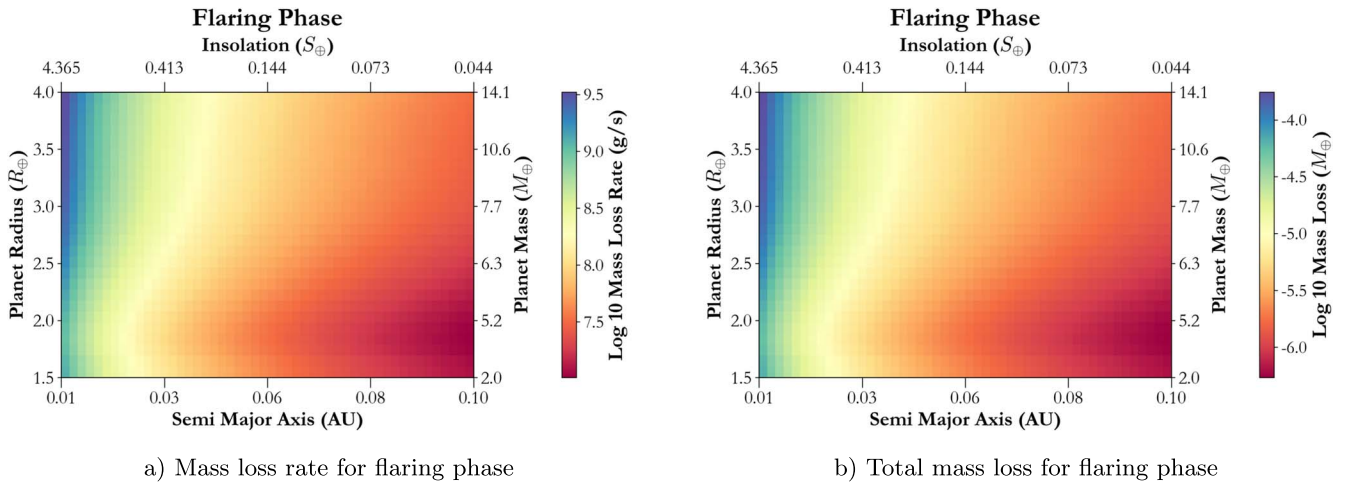


**Figure 11.** The atmospheric mass loss across a range of small planet radii ( $1.5\text{--}4 R_{\oplus}$ ), and semimajor axis spanning 0.01–0.1 au using Equation (1). (a) The rate of mass loss, assuming a high-energy luminosity ( $L_{\text{HE}} = 10^{27} \text{ erg s}^{-1}$ ) equivalent to Fleming et al. (2000). To calculate the insolation at different separations for vB 10, we use the bolometric luminosity of  $\log L_{\text{bol}} = -3.36$  (Tinney et al. 1993). (b) We propagate the mass-loss rate over 1 Gyr to calculate the cumulative atmospheric mass loss for a small planet around vB 10, with a flare duration of 1 hr and frequency of once per 100 hr, as estimated in Section 6.3. As discussed in Section 6.4, the mass loss during the quiescent phases should be approximately double the loss from such flares. The relatively low mass-loss rate estimated for vB 10 is consistent with its low  $v \sin i$  and is likely to have been higher earlier in its lifetime.

“recovered” if it occurs during a time matching a time stamp from our HPF time series. After all 10,000 trials, the numbers of “recovered” flares are then organized into a histogram to determine the peak number of recovered flares for a given wait time. To avoid double counting where two data points may occur within one flare, a flare is no longer counted in that series/trial once one data point is found to occur within the flare. In this case, we looked for a peak of one recovered flare, just before the peak transitions to two. At this point, the wait time is the maximum flare frequency (or, in other words, the star cannot flare more often than wait time days). Therefore, for a flare duration of 1 hr (Paudel et al. 2018), we obtain a maximum flare frequency of once every 2.5 days (or 60 hr). This upper limit to the frequency is consistent with the estimate of  $\sim 100$  hr based on the scaling from the K2 ultracool dwarf flare observations (Paudel et al. 2018).

#### 6.4. Implication for Photoevaporation

Atmospheres of close-in exoplanets are susceptible to photoevaporation due to high-energy ionizing radiation (Owen & Jackson 2012). Similar EUV and X-ray radiation has been reported for vB 10, during both quiescent (Fleming et al. 2003) and flaring phases (Linsky et al. 1995; Fleming et al. 2000; Berger et al. 2008). We attempt to place limits on the mass-loss rates of a hypothetical small planet ( $R_p < 4 R_{\oplus}$ ) across a range of radii and separation from the star, using a simplified version of the formalism from Erkaev et al. (2007), Penz & Micela (2008), and Owen & Jackson (2012) to estimate the mass-loss rate ( $\dot{M}$ ):

$$\dot{M} = \frac{\pi R_p^3 L_{\text{HE}}}{GM_p 4\pi a^2}, \quad (1)$$

where  $R_p$  and  $M_p$  are the planetary radius and mass, respectively,  $a$  represents the semimajor axis,  $G$  is the gravitational constant, and  $L_{\text{HE}}$  is the high-energy ionizing radiation luminosity. We use the  $M_{\text{REXO}}$  (Kanodia et al. 2019) mass–radius relation for M dwarf planets, to predict planetary masses for a range of radii. We are unable to constrain the EUV

emission for vB 10 with our data spanning the decay phase of this flare. However, we expect the early stages of this flare to be accompanied by high-energy EUV and X-ray radiation based on previous flare observations of vB 10. We calculate the mass-loss rate over 1 Gyr for two cases: (i) using the estimates for frequencies of such flares from our observations and an  $L_{\text{HE}}$  equivalent to the X-ray flare reported by Fleming et al. (2000) ( $L_{\text{HE}} = 10^{27} \text{ erg s}^{-1}$ ) as an upper limit (Figure 11), and (ii) using the quiescent X-ray luminosity of  $2 \times 10^{25} \text{ erg s}^{-1}$ , as reported by Fleming et al. (2003) and Berger et al. (2008). In the first case, we use the flare frequency of once every 100 hr (Section 6.3) and a duration of 1 hr (based on Paudel et al. 2018), i.e., a duty cycle of  $\sim 1\%$  (this is consistent with the  $3\% \pm 1\%$  duty cycle estimated by Hilton 2011 for the M7–M9 spectral subtype). Conversely, in the case of quiescent high-energy radiation, the X-ray luminosity is about 1/50 that of the flares. Given the 1% duty cycle for such flares and the characteristics stated above, the mass loss during the quiescent phase should be higher ( $2 \times$ ) than that from the flaring phase.

For reference, according to the planetary models from Lopez & Fortney (2014), the atmospheric envelope mass fraction for sub-Neptune in the radius valley (Fulton et al. 2017) with radius =  $1.7 R_{\oplus}$ , mass =  $3.4 M_{\oplus}$  and insolation of  $1 S_{\oplus}$  (semimajor axis = 0.02 au) should be 0.2%, or an atmospheric mass of  $7 \times 10^{-3} M_{\oplus}$ . Therefore, the total atmospheric mass loss over a Gyr is 0.5% of the atmospheric mass given similar flares (Figure 11). Using this hypothetical sub-Neptune in the habitable zone of vB 10 as an example, we place limits on the atmospheric mass loss from flaring and quiescent high-energy radiation.

We include the caveat that we have assumed the rate of radiation to be constant with stellar age in this work. vB 10 has a low  $v \sin i$  (Reiners et al. 2018) and is likely to have been more active with more frequent flares, and had a higher  $L_{\text{X}}/L_{\text{bol}}$  when it was younger (Paudel et al. 2018, 2019; McDonald et al.

2019), resulting in a larger mass-loss rate.<sup>34</sup> vB 10 was not observed by the Kepler or K2 mission, but it will be observed by TESS in Cycle 4 during Sector 54 (2022 July). This will help place better limits on the flare rate as a function of energy for vB 10, similar to work from Feinstein et al. (2020), which will also be useful to constrain planetary atmospheric losses due to photoevaporation.

## 7. Conclusion

In this work, we present observations of a flare around the ultracool M8 dwarf vB 10, which include high-resolution NIR spectra from HPF, as well as photometry from the acquisition camera (ACAM) on HET. We draw the following conclusions based on the HPF spectra:

1. We use the HPF spectra to measure emission in the calcium IRT, Paschen lines, the He  $\lambda$ 10830 triplet, and iron and magnesium lines.
2. We present evidence for observations of coronal rain on this star, which is not only the first time it has been observed on such a late-type star but also the first time it has been observed in the He I triplet for M dwarfs. This is in the form of an asymmetry in the He I triplet,  $\sim 70$  km s<sup>-1</sup> redward of the primary lines, as well as tentative evidence of a similar asymmetry for the Pa 6 ( $\gamma$ ) line.
3. We flux-calibrate the HPF spectra and estimate the absolute flux emitted in the various lines during the flare. We also note that the calcium, Paschen, and helium lines are consistent with being optically thick.
4. Utilizing the NDR capability of the HPF detector, we reconstruct the temporal evolution during the gradual decay phase of the flare.

The large HET aperture ( $\sim 10$  m) allows for high-resolution spectral observations of this ultracool faint dwarf, which help place strict upper limits ( $|v| < 5$  km s<sup>-1</sup>) on the velocity offsets of the emission features in the spectra. Detailed hydrodynamic modeling of the atmospheres of these faint ultracool dwarfs, with their molecular hazes at low  $T_{\text{eff}}$ , is notoriously difficult. However, ongoing RV surveys should provide for serendipitous flare observations similar to those presented here, which should help extend the models to these lower temperatures.

We measure a continuum enhancement in the ACAM photometry, which we use to calculate the bolometric luminosity of the flare assuming a 10,000 K blackbody. We estimate that at its peak the flare had a bolometric luminosity  $\sim 70\%$  that of the star itself! Using scaling relations developed from K2 observations of ultracool dwarfs, we also estimate the frequency of similar flares around vB 10. Finally, we discuss the XUV radiation that is released during such flares and its impact on the atmospheric evolution of planets.

We thank the anonymous referees for their helpful feedback.

This research has made use of the SIMBAD database, operated at CDS, Strasbourg, France, and NASA's Astrophysics Data System Bibliographic Services.

Computations for this research were performed on the Pennsylvania State University's Institute for Computational and Data Sciences Advanced CyberInfrastructure (ICDS-ACI),

including the CyberLAMP cluster supported by NSF grant MRI-1626251.

The Center for Exoplanets and Habitable Worlds is supported by the Pennsylvania State University, the Eberly College of Science, and the Pennsylvania Space Grant Consortium.

This work has made use of data from the European Space Agency (ESA) mission Gaia (<https://www.cosmos.esa.int/gaia>), processed by the Gaia Data Processing and Analysis Consortium (DPAC, <https://www.cosmos.esa.int/web/gaia/dpac/consortium>). Funding for the DPAC has been provided by national institutions, in particular the institutions participating in the Gaia Multilateral Agreement.

These results are based on observations obtained with the Habitable-zone Planet Finder Spectrograph on the HET. We acknowledge support from NSF grants AST-1006676, AST-1126413, AST-1310885, AST-1310875, AST-1910954, AST-1907622, AST-1909506, ATI 2009889, ATI-2009982, and AST-2108512 and the NASA Astrobiology Institute (NNA09-DA76A) in the pursuit of precision RVs in the NIR. The HPF team also acknowledges support from the Heising-Simons Foundation via grant 2017-0494. The Hobby-Eberly Telescope is a joint project of the University of Texas at Austin, the Pennsylvania State University, Ludwig-Maximilians-Universität München, and Georg-August Universität Göttingen. The HET is named in honor of its principal benefactors, William P. Hobby and Robert E. Eberly. The HET collaboration acknowledges the support and resources from the Texas Advanced Computing Center. We thank the resident astronomers and telescope operators at the HET for the skillful execution of our observations with HPF. We would like to acknowledge that the HET is built on Indigenous land. Moreover, we would like to acknowledge and pay our respects to the Carrizo & Comecrudo, Coahuiltecan, Caddo, Tonkawa, Comanche, Lipan Apache, Alabama-Coushatta, Kickapoo, Tigua Pueblo, and all the American Indian and Indigenous Peoples and communities who have been or have become a part of these lands and territories in Texas, here on Turtle Island.

This work includes data from 2MASS, which is a joint project of the University of Massachusetts and IPAC at Caltech funded by NASA and the NSF. C.I.C. acknowledges support by NASA Headquarters under the NASA Earth and Space Science Fellowship Program through grant 80NSSC18K1114. S.K. would like to acknowledge Annie Clark and Theodora for help with this project.

*Facilities:* Gaia, HET (HPF).

*Software:* AstroImageJ (Collins et al. 2017), astropy (Robitaille et al. 2013; Astropy Collaboration et al. 2018), astroquery (Ginsburg et al. 2019), barycorrpy (Kanodia & Wright 2018), ccdproc (Craig et al. 2017), HxRGproc (Ninan et al. 2018), ipython (Pérez & Granger 2007), matplotlib (Hunter 2007), numpy (Oliphant 2006), pandas (McKinney 2010), photutils (Bradley et al. 2020), scipy (Oliphant 2007; Virtanen et al. 2020), telfit (Gullikson et al. 2014) terraspec (Bender et al. 2012; Lockwood et al. 2014).

<sup>34</sup> Furthermore, for simplicity we do not consider the Roche lobe effects discussed by Erkaev et al. (2007) in these calculations.

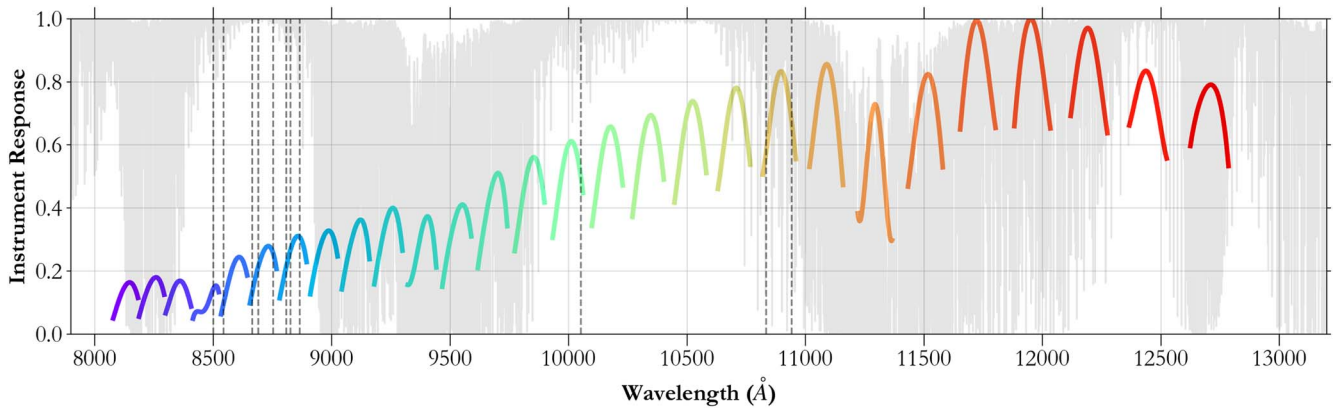


**Figure 12.** The relative instrument response as a function of wavelength. The dashed lines mark the positions of the lines considered in this analysis (Table 2). Note the irregularly shaped HPF instrument response in the wavelength region spanning the first two IRT lines (Order Index 3–4;  $\sim 8490$ – $8550$  Å), which is attributed to an absorption band in the multilayer HPF mirror coating. The shaded spectrum in the background is a representative telluric model generated from `TelFit` (Gullikson et al. 2014). This indicates the regions of heavy telluric absorption that reduce the local instrument response in particular orders.

## Appendix A Spectral Reduction and Correction

### A.1. Telluric Correction

We perform telluric correction on the sky-subtracted spectrum following a procedure similar to Robertson et al. (2016). We use the sky-subtracted spectrum after correcting for the intraorder (and interorder) instrument response (Section A.3). The telluric correction is performed using the `TERRASPEC` code (Bender et al. 2012; Lockwood et al. 2014), which uses the `LBLRTM` radiative transfer code (Clough et al. 2005) to generate a synthetic telluric absorption function that calculates a telluric model using an observer’s altitude, target zenith angle, and telluric conditions integrated over a given science observation. `LBLRTM` uses the `HITRAN 2012` database of molecular lines (Rothman et al. 2013) and can access a variety of standard atmospheric models. The telluric absorption function is combined in a forward model with the instrument profile, which we parameterize as a series of overlapping Gaussian functions (e.g., Valenti et al. 1995; Endl et al. 2000). We use nonlinear least-squares minimization (Markwardt 2009) to optimize the integrated column depths of the atmospheric molecules and instrument profile parameters to best match the observed science spectrum. To process the HPF spectrum, we used the US standard atmospheric model (National 1992), with the instrument profile as described above. We use the water-dominated telluric regions in our spectrum to get initial values for water column depth and instrument profile. We then use this as the initial values for each order-by-order fit to the HPF spectrum. We opt to fit each order separately to account for any slight changes in the instrument point-spread function (PSF) as the wavelength increases. However, there are still wavelength regions that are quite heavily contaminated by tellurics (mainly water vapor), and they are shown in Figure 12 as the shaded spectrum.

In addition to the telluric absorption correction, we also perform a sky subtraction to correct for hydroxyl radical OH sky emission lines using the simultaneous sky spectrum obtained by HPF’s sky fiber (Kanodia et al. 2018). Correction of the sky emission features is especially important for the He  $\lambda 10830$  region and is performed by scaling and subtracting the sky spectrum from the science spectrum (Ninan et al. 2020).

### A.2. Velocity Correction

The telluric-corrected spectrum is shifted to the solar system barycentric frame using `barycorrpy` (Kanodia & Wright 2018), the Python implementation of the algorithms from Wright & Eastman (2014). We estimate the absolute RV of vB 10 to be  $35.5 \text{ km s}^{-1}$ , which is calculated by stepping the vB 10 spectrum against the HPF spectrum of GJ 699 (after shifting the GJ 699 spectrum to the stellar rest frame) in velocity space and minimizing the  $\chi^2$ . This is consistent with the absolute RV from estimates from Mohanty & Basri (2003), Zapatero Osorio et al. (2009), Reiners et al. (2018), and also the Gaia DR2 measurement for GJ 752 A<sup>35</sup> (the brighter binary companion).

### A.3. Relative Instrument Response Calibration

To estimate the ratios of flux emitted across different lines, we need to correct for the intraorder instrument response variation due to the grating blaze function, as well as the interorder overall chromatic instrument response. In addition to the grating blaze function, for HPF order index 3 ( $\sim 8410$ – $8530$  Å), we also see a higher-order chromatic effect that is attributed to a flaw in the multilayer reflection coating in HPF (Figure 12). We also need the flux calibration to convert from measured photoelectrons to spectral flux density units ( $\text{erg s}^{-1} \text{ cm}^{-2} \text{ Å}^{-1}$ ).

We first modeled the HPF spectrum of the A0 star HR 3437 with a  $v \sin i$  broadened<sup>36</sup> model spectrum of Vega (Castelli & Kurucz 1994). The broadened model spectrum was interpolated onto the stellar wavelength grid and then divided from the HPF spectrum. The ratio (stellar to model) spectrum represents the relative instrument response and was fit using 4th-degree Chebyshev polynomials (Chebyshev 1854). The converging Paschen series<sup>37</sup> (Paschen 1908) of lines (Kramida 2010; Kramida et al. 2020) in this spectrum of HR 3437 are not accurately modeled by the Vega spectrum and hence need to be masked. Despite the masking, lines at the edges of the HPF orders skew the response fit and prevent robust unbiased estimation of the instrument response.

<sup>35</sup> Note that there are no Gaia RV estimates for the bulk velocity of vB 10.

<sup>36</sup>  $v \sin i$  broadening of  $193 \text{ km s}^{-1}$  (Díaz et al. 2011).

<sup>37</sup> Atomic hydrogen transitions to the  $n = 3$  level, with  $\lambda_{n\infty} = 8207$  Å (vacuum; air = 8204 Å).

We then used HPF observations of the G3 dwarf star 16 Cyg B, alongside the CALSPEC model spectrum for the same target (Bohlin et al. 2014, 2020). The CALSPEC model spectrum does not require  $v \sin i$  broadening and was interpolated onto the stellar wavelength grid and then normalized to 1. The ratio of stellar to model flux is then median smoothed with a kernel of 101 pixels and fit with a Chebyshev polynomial after masking the Paschen lines, similar to before. This gives a more unbiased estimate of the instrument response than the A0 spectrum, primarily because the Paschen lines in 16 Cyg B are not broadened to the same extent as the A0 stars, with much lesser rotational, temperature, and pressure broadening (Gray 1992).

This procedure gives us the relative instrument response that corrects for the inter- and intraorder response variation and converts the measured HPF spectrum from electrons to spectral flux density units. To account for varying atmospheric extinction due to changing water vapor and dust levels between the epoch corresponding to the flare observations and that for the 16 Cyg B observations, we conservatively assume a  $\sim 10\%$  error. This is based on observations of CALSPEC flux standards to estimate the HPF instrument response, where we note relative chromatic trends at  $\sim 10\%$  across the response calculated for the HPF bandpass across observations that are temporally spaced by more than a few minutes. Additionally, we also include a 10% error term to account for inaccuracies in the interorder normalization while correcting the instrument response. Adding these individual error terms in quadrature, we ascribe an error of 15% to our response corrections per extracted pixel.

#### A.4. Absolute Calibration

We also scale the response-corrected  $vB$  10 spectrum to  $3.435 \times 10^{-14} \text{ erg s}^{-1} \text{ cm}^{-2} \text{ \AA}^{-1}$ , corresponding to its 2MASS  $J$  magnitude of 9.9 at 12350  $\text{\AA}$  (Cutri et al. 2003). Doing this enables us to estimate the absolute flux (and therefore energy) emitted in specific atomic lines during the flare. Here we make the assumption that the bolometric luminosity of  $vB$  10 remains constant between the epoch of 2MASS observations in 2003 (Cutri et al. 2003) and the  $vB$  10 flares as observed by HPF.

#### A.5. Spectral Subtraction

The complexity of the late M dwarf spectrum and lack of real continuum for any equivalent-width-like measurements led us to adopt the spectral subtraction method to quantify the emission flux during the flare (Paulson et al. 2006). We normalize and take the weighted average for  $2 \times 945$  s exposures of  $vB$  10 from 2018 September 24, 03:19 UTC in the stellar rest frame, as a quiescent epoch reference spectrum. This spectrum is telluric corrected, similar to the flare spectrum described in Section 3. Before subtraction, both the flare and quiescent spectrum are normalized, instrument response corrected, and flux-calibrated using the procedure described in Sections A.3 and A.4. An example of this is shown for the Pa 7 ( $\delta$ ) line in Figure 13, where we note that the Pa (and similarly the Ca or He) lines can get obscured in the molecular haze for such an ultracool dwarf and are not observed to be in strong absorption during quiescence. Since HPF is a highly stabilized spectrograph with a scrambled fiber input (Halverson et al. 2015), we can perform this subtraction without accruing errors

from variable seeing conditions (between the reference and flare epochs) or guiding jitter (Kanodia et al. 2021).

## Appendix B ACAM Photometry Reduction

All ACAM frames were 2D bias and dark subtracted. In addition, we reject cosmic rays using the L.A. Cosmic technique (van Dokkum 2001), which uses the Laplacian edge detection as implemented in `ccdproc` (Craig et al. 2017). We also correct for column pattern noise in the detector, by masking out the sources and then subtracting the masked mean value from each column. An approximate world coordinate system (WCS) is available in the header in the form of the telescope R.A. and decl., but that does not take into account the orientation of the guide camera. In the case of the ACAM, we find that packages like `astrometry.net` (Lang et al. 2010) fail in finding a plate solution due to a combination of the small field of view, limiting magnitude, and the movement of high proper-motion targets in the field. A more accurate WCS plate solution is added to the headers by detecting sources in the images and comparing them to the Gaia DR2 catalog (Gaia Collaboration et al. 2018) within a  $5'$  radius using `astroquery` (Ginsburg et al. 2019). This subset of the Gaia catalog is propagated to the epoch of observation by applying space motion, and a transformation from the detected pixel positions to Gaia positions is applied to obtain a WCS solution. These images were filtered out by eye based on threshold count values described below. In addition, we also filtered out double images with a moving field of view, low peak counts in the target star ( $< 7000$  counts), and background sky overexposure ( $> 1000$  counts). A multiaperture photometric data analysis was completed using the Java-based image processing software AstroImageJ (AIJ; Collins et al. 2017). We use a photometric aperture of 12 pixels ( $3''.25$ ) with an inner sky annulus of 21 pixels ( $5''.69$ ) and outer sky annulus of 32 pixels ( $8''.67$ ), which were selected based on the PSF FWHM of the target star.

## ORCID iDs

Shubham Kanodia  <https://orcid.org/0000-0001-8401-4300>  
 Lawrence W. Ramsey  <https://orcid.org/0000-0002-4289-7958>  
 Marissa Maney  <https://orcid.org/0000-0001-8222-9586>  
 Suvrath Mahadevan  <https://orcid.org/0000-0001-9596-7983>  
 Caleb I. Cañas  <https://orcid.org/0000-0003-4835-0619>  
 Joe P. Ninan  <https://orcid.org/0000-0001-8720-5612>  
 Andrew Monson  <https://orcid.org/0000-0002-0048-2586>  
 Adam F. Kowalski  <https://orcid.org/0000-0001-7458-1176>  
 Gudmundur Stefansson  <https://orcid.org/0000-0001-7409-5688>  
 Chad F. Bender  <https://orcid.org/0000-0003-4384-7220>  
 William D. Cochran  <https://orcid.org/0000-0001-9662-3496>  
 Scott A. Diddams  <https://orcid.org/0000-0002-2144-0764>  
 Connor Fredrick  <https://orcid.org/0000-0002-0560-1433>  
 Samuel Halverson  <https://orcid.org/0000-0003-1312-9391>  
 Fred Hearty  <https://orcid.org/0000-0002-1664-3102>  
 Steven Janowiecki  <https://orcid.org/0000-0001-9165-8905>  
 Andrew J. Metcalf  <https://orcid.org/0000-0001-5000-1018>  
 Paul Robertson  <https://orcid.org/0000-0003-0149-9678>  
 Arpita Roy  <https://orcid.org/0000-0001-8127-5775>

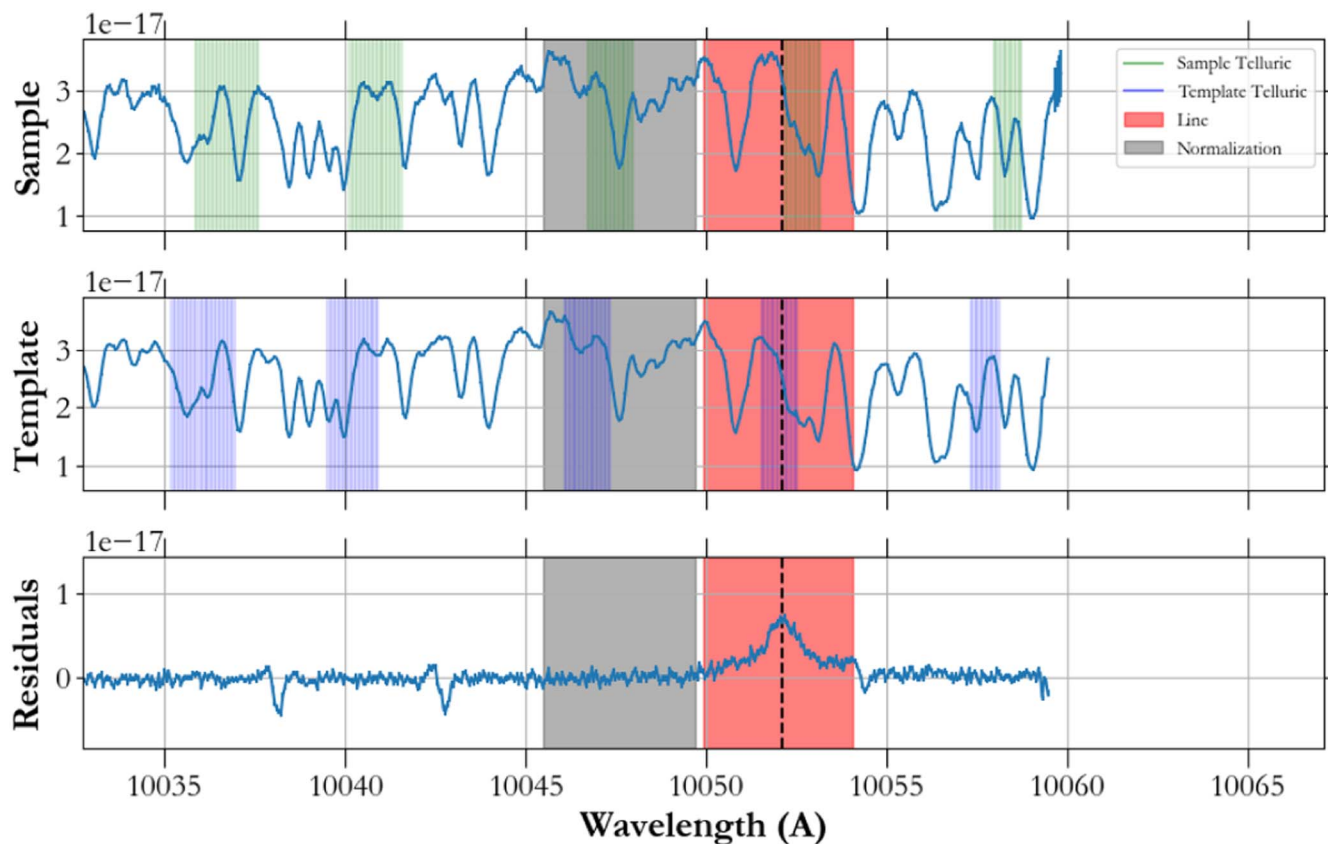


**Figure 13.** An example of the spectral subtraction, with the sample spectrum shown in the top panel, the template in the middle panel, and the residuals in the bottom panel. While the excess at the position of the Pa 7 ( $\delta$ ) line is apparent in the residual spectrum, it is harder to tease out before subtracting a quiescent template.

Christian Schwab <https://orcid.org/0000-0002-0091-7105>

Ryan C. Terrien <https://orcid.org/0000-0002-4788-8858>

## References

- Allard, F., Homeier, D., & Freytag, B. 2012, *RSPTA*, 370, 2765
- Antolin, P., & Rouppe van der Voort, L. 2012, *ApJ*, 745, 152
- Astropy Collaboration, Price-Whelan, A. M., Sipőcz, B. M., et al. 2018, *AJ*, 156, 123
- Batalha, N. E., Lewis, T., Fortney, J. J., et al. 2019, *ApJL*, 885, L25
- Bender, C. F., Mahadevan, S., Deshpande, R., et al. 2012, *ApJ*, 751, L31
- Berger, E., Basri, G., Gizis, J. E., et al. 2008, *ApJ*, 676, 1307
- Bohlin, R. C., Gordon, K. D., & Tremblay, P.-E. 2014, *PASP*, 126, 711
- Bohlin, R. C., Hubeny, I., & Rauch, T. 2020, *AJ*, 160, 21
- Bradley, L., Sipőcz, B., Robitaille, T., et al. 2020, *astropy/photutils*: 1.0.0, Zenodo doi:[10.5281/zenodo.4044744](https://doi.org/10.5281/zenodo.4044744)
- Canfield, R. C., Penn, M. J., Wulser, J.-P., & Kiplinger, A. L. 1990, *ApJ*, 363, 318
- Castelli, F., & Kurucz, R. L. 1994, *A&A*, 281, 817
- Chang, S. W., Byun, Y. I., & Hartman, J. D. 2015, *ApJ*, 814, 35
- Chebyshev, P. L. 1854, *Mémoires Présentés à l'Académie Impériale des Sciences de St-Petersbourg par Divers Savants*, 7, 539
- Clough, S. A., Shephard, M. W., Mlawer, E. J., et al. 2005, *JQSRT*, 91, 233
- Collaboration, G., Brown, A. G. A., Vallenari, A., et al. 2021, *A&A*, 649, A1
- Collins, K. A., Kielkopf, J. F., Stassun, K. G., & Hessman, F. V. 2017, *AJ*, 153, 77
- Craig, M., Crawford, S., Seifert, M., et al. 2017, *astropy/ccdproc*: v1.3.0.post1, Zenodo doi:[10.5281/zenodo.1069648](https://doi.org/10.5281/zenodo.1069648)
- Crespo-Chacón, I., Montes, D., García-Alvarez, D., et al. 2006, *A&A*, 452, 987
- Cuntz, M., & Guinan, E. F. 2016, *ApJ*, 827, 79
- Cutri, R. M., Skrutskie, M. F., van Dyk, S., et al. 2003, *The IRSA 2MASS All-Sky Point Source Catalog*, NASA/IPAC Infrared Science Archive
- Díaz, C. G., González, J. F., Levato, H., & Grosso, M. 2011, *A&A*, 531, A143
- Donati, J. F., Kouch, D., Moutou, C., et al. 2020, *MNRAS*, 498, 5684
- Dressing, C. D., & Charbonneau, D. 2015, *ApJ*, 807, 45
- Endl, M., Kürster, M., & Els, S. 2000, *A&A*, 362, 585
- Erkaev, N. V., Kulikov, Y. N., Lammer, H., et al. 2007, *A&A*, 472, 329
- Feinstein, A. D., Montet, B. T., Ansdell, M., et al. 2020, *AJ*, 160, 219
- Fleming, T. A., Giampapa, M. S., & Garza, D. 2003, *ApJ*, 594, 982
- Fleming, T. A., Giampapa, M. S., & Schmitt, J. H. M. M. 2000, *ApJ*, 533, 372
- Fouqué, P., Moutou, C., Malo, L., et al. 2018, *MNRAS*, 475, 1960
- Fuhrmeister, B., Czesla, S., Hildebrandt, L., et al. 2020, *A&A*, 640, A52
- Fuhrmeister, B., Czesla, S., Schmitt, J. H. M. M., et al. 2018, *A&A*, 615, A14
- Fuhrmeister, B., Czesla, S., Schmitt, J. H. M. M., et al. 2019, *A&A*, 623, A24
- Fuhrmeister, B., Lalitha, S., Poppenhaeger, K., et al. 2011, *A&A*, 534, A133
- Fuhrmeister, B., Liefke, C., & Schmitt, J. H. M. M. 2007, *A&A*, 468, 221
- Fuhrmeister, B., Liefke, C., Schmitt, J. H. M. M., & Reiners, A. 2008, *A&A*, 487, 293
- Fulton, B. J., Petigura, E. A., Howard, A. W., et al. 2017, *AJ*, 154, 109
- Gaia Collaboration, Brown, A. G. A., Vallenari, A., et al. 2018, *A&A*, 616, A1
- Ginsburg, A., Sipőcz, B. M., Brasseur, C. E., et al. 2019, *AJ*, 157, 98
- Gizis, J. E., Burgasser, A. J., Berger, E., et al. 2013, *ApJ*, 779, 172
- Gizis, J. E., Paudel, R. R., Mullan, D., et al. 2017, *ApJ*, 845, 33
- Graham, D. R., & Cauzzi, G. 2015, *ApJ*, 807, L22
- Graham, D. R., Cauzzi, G., Zangrilli, L., et al. 2020, *ApJ*, 895, 6
- Gray, D. F. 1992, *Camb. Astrophys. Ser.*, Vol. 20 (Cambridge: Cambridge Univ. Press)
- Guedel, M., & Benz, A. O. 1993, *ApJ*, 405L, 63G
- Gullikson, K., Dodson-Robinson, S., & Kraus, A. 2014, *AJ*, 148, 53
- Hall, J. C., & Ramsey, L. W. 1992, *AJ*, 104, 1942
- Halverson, S., Roy, A., Mahadevan, S., et al. 2015, *ApJ*, 806, 61
- Hardegree-Ullman, K. K., Cushing, M. C., Muirhead, P. S., & Christiansen, J. L. 2019, *AJ*, 158, 75
- Henry, T. J., Jao, W.-C., Subasavage, J. P., et al. 2006, *AJ*, 132, 2360
- Herbig, G. H. 1956, *PASP*, 68, 531
- Hilton, E. J. 2011, PhD thesis, Univ. Washington
- Honda, S., Notsu, Y., Namekata, K., et al. 2018, *PASJ*, 70, 62
- Hunter, J. D. 2007, *CSE*, 9, 90
- Ichimoto, K., & Kurokawa, H. 1984, *SoPh*, 93, 105
- Irwin, J. M., Berta-Thompson, Z. K., Charbonneau, D., et al. 2015, in 18th Cambridge Workshop on Cool Stars, Stellar Systems, and the Sun, ed. G. van Belle & H. C. Harris (Ann Arbor, MI: Univ. Michigan)

- Johns-Krull, C. M., Hawley, S. L., Basri, G., & Valenti, J. A. 1997, *ApJS*, **112**, 221
- Joy, A. H., & Humason, M. L. 1949, *PASP*, **61**, 133
- Judge, P. G., Kleint, L., & Sainz Dalda, A. 2015, *ApJ*, **814**, 100J
- Kahler, S., Golub, L., Harnden, F. R., et al. 1982, *ApJ*, **252**, 239
- Kanodia, S., Halverson, S., Ninan, J. P., et al. 2021, *ApJ*, **912**, 15
- Kanodia, S., Mahadevan, S., Ramsey, L. W., et al. 2018, *Proc. SPIE*, **0702**, 107026Q
- Kanodia, S., Wolfgang, A., Stefansson, G. K., Ning, B., & Mahadevan, S. 2019, *ApJ*, **882**, 38
- Kanodia, S., & Wright, J. 2018, *RNAAS*, **2**, 4
- Kirkpatrick, J. D., Henry, T. J., & Simons, D. A. 1995, *AJ*, **109**, 797
- Kotani, T., Tamura, M., Nishikawa, J., et al. 2018, *Proc. SPIE*, **0702**, 1070211
- Kowalski, A. F., Hawley, S. L., Carlsson, M., et al. 2015, *SoPh*, **290**, 3487
- Kowalski, A. F., Hawley, S. L., Wisniewski, J. P., et al. 2013, *ApJS*, **207**, 15
- Kowalski, A. F., Wisniewski, J. P., Hawley, S. L., et al. 2019, *ApJ*, **871**, 167
- Kramida, A. E. 2010, *ADNDT*, **96**, 586
- Kramida, A. E., Ralchenko, Yu., Reader, J. & NIST ASD Team. 2020, NIST Atomic Spectra Database (ver. 5.8) (Gaithersburg, MD: National Institute of Standards and Technology) <https://physics.nist.gov/asd>
- Kunkel, W. E. 1970, *ApJ*, **161**, 503
- Lacatus, D. A., Judge, P. G., & Donea, A. 2017, *ApJ*, **842**, 15
- Lacy, C. H., Moffett, T. J., & Evans, D. S. 1976, *ApJS*, **30**, 85L
- Landman, D. A., & Illing, R. M. E. 1977, *A&A*, **55**, 103
- Lang, D., Hogg, D. W., Mierle, K., Blanton, M., & Roweis, S. 2010, *AJ*, **139**, 1782
- Li, C., Zhong, S. J., Xu, Z. G., et al. 2018, *MNRAS*, **479**, L139
- Liebert, J., Kirkpatrick, J. D., Reid, I. N., & Fisher, M. D. 1999, *ApJ*, **519**, 345
- Liebert, J., Kron, R. G., & Spinrad, H. 1978, *PASP*, **90**, 718
- Linsky, J. L., Wood, B. E., Brown, A., Giampapa, M. S., & Ambruster, C. 1995, *ApJ*, **455**, 670
- Lockwood, A. C., Johnson, J. A., Bender, C. F., et al. 2014, *ApJ*, **783**, L29
- Lopez, E. D., & Fortney, J. J. 2014, *ApJ*, **792**, 1
- Luger, R., Barnes, R., Lopez, E., et al. 2015, *AsBio*, **15**, 57
- Mahadevan, S., Ramsey, L., Bender, C., et al. 2012, *Proc. SPIE*, **8446**, 84461S
- Mahadevan, S., Ramsey, L. W., Terrien, R., et al. 2014, *Proc. SPIE*, **9147**, 91471G
- Markwardt, C. B. 2009, in *Astronomical Data Analysis Software and Systems XVIII ASP Conf. Ser.* 411, **411** (San Francisco, CA: ASP), 251
- Martin, E. L. 1999, *MNRAS*, **302**, 59
- Martin, J., Fuhrmeister, B., Mittag, M., et al. 2017, *A&A*, **605**, A113
- McDonald, G. D., Kreidberg, L., & Lopez, E. 2019, *ApJ*, **876**, 22
- McKinney, W. 2010, in *Proc. of the 9th Python in Science Conf.*, ed. S. v. d. Walt & J. Millman (Austin, TX: SciPy), 56
- Metcalf, A. J., Anderson, T., Bender, C. F., et al. 2019, *Optica*, **6**, 233
- Mochnacki, S. W., & Zirin, H. 1980, *ApJ*, **239**, L27
- Mohanty, S., & Basri, G. 2003, *ApJ*, **583**, 451
- Montes, D., Fernández-Figueroa, M. J., De Castro, E., et al. 2000, *A&AS*, **146**, 103
- Muheki, P., Guenther, E. W., Mutabazi, T., & Jurua, E. 2020, *A&A*, **637**, A13
- Mulders, G. D., Pascucci, I., & Apai, D. 2015, *ApJ*, **798**, 112
- National, C. G. D. 1992, *P&SS*, **40**, 553
- Neidig, D. F., & Wiborg, P. H., Jr. 1984, *SoPh*, **92**, 217
- Ninan, J. P., Bender, C. F., Mahadevan, S., et al. 2018, *Proc. SPIE*, **10709**, 107092U
- Ninan, J. P., Stefansson, G., Mahadevan, S., et al. 2020, *ApJ*, **894**, 97
- Oliphant, T. 2006, *NumPy: A guide to NumPy (USA: Trelgol Publishing)*
- Oliphant, T. E. 2007, *CSE*, **9**, 10
- Osten, R. A., Kowalski, A., Sahu, K., & Hawley, S. L. 2012, *ApJ*, **754**, 4
- Osterbrock, D. E. 1989, *Astrophysics of Gaseous Nebulae and Active Galactic Nuclei* (Sausalito, CA: University Science Books)
- Owen, J. E., & Jackson, A. P. 2012, *MNRAS*, **425**, 2931
- Owen, J. E., & Mohanty, S. 2016, *MNRAS*, **459**, 4088
- Paschen, F. 1908, *AnP*, **332**, 537
- Paudel, R. R., Gizis, J. E., Mullan, D. J., et al. 2018, *ApJ*, **858**, 55
- Paudel, R. R., Gizis, J. E., Mullan, D. J., et al. 2019, *MNRAS*, **486**, 1438
- Paulson, D. B., Allred, J. C., Anderson, R. B., et al. 2006, *PASP*, **118**, 227
- Penz, T., & Micela, G. 2008, *A&A*, **479**, 579
- Pérez, F., & Granger, B. E. 2007, *CSE*, **9**, 21
- Pettersen, B. R., & Hawley, S. L. 1989, *A&A*, **217**, 187
- Quirrenbach, A., Amado, P. J., Caballero, J. A., et al. 2014, *Proc. SPIE*, **9147**, 91471F
- Ramsay, G., Kolotkov, D., Doyle, J. G., & Doyle, L. 2021, *SoPh*, **296**, 162
- Ramsey, L. W., Adams, M. T., Barnes, T. G., et al. 1998, *Proc. SPIE*, **3352**, 34
- Reid, I. N., & Hawley, S. L. 2000, *New Light on Dark Stars: Red Dwarfs* (Chichester: Praxis Publishing)
- Reiners, A., Zechmeister, M., Caballero, J. A., et al. 2018, *A&A*, **612**, A49
- Ricker, G. R., Winn, J. N., Vanderspek, R., et al. 2014, *JATIS*, **1**, 014003
- Robertson, P., Bender, C., Mahadevan, S., Roy, A., & Ramsey, L. W. 2016, *ApJ*, **832**, 112
- Robitaille, T. P., Tollerud, E. J., Greenfield, P., et al. 2013, *A&A*, **558**, A33
- Rothman, L. S., Gordon, I. E., Babikov, Y., et al. 2013, *JQSRT*, **130**, 4
- Ruan, W., Zhou, Y., & Keppens, R. 2021, *ApJL*, **920**, L15
- Scalo, J., Kaltenecker, L., Segura, A., et al. 2007, *AsBio*, **7**, 85
- Schmidt, S. J., Cruz, K. L., Bongiorno, B. J., Liebert, J., & Reid, I. N. 2007, *AJ*, **133**, 2258
- Schmidt, S. J., Kowalski, A. F., Hawley, S. L., et al. 2012, *ApJ*, **745**, 14
- Schöfer, P., Jeffers, S. V., Reiners, A., et al. 2019, *A&A*, **623**, A44
- Seifahrt, A., Bean, J. L., Stürmer, J., et al. 2016, *Proc. SPIE*, **9908**, 990818
- Stefansson, G., Hearty, F., Robertson, P., et al. 2016, *ApJ*, **833**, 175
- Tinney, C. G., Reid, I. N., & Mould, J. R. 1993, *ApJ*, **414**, 254
- Valenti, J. A., Butler, R. P., & Marcy, G. W. 1995, *PASP*, **107**, 966
- van Biesbroeck, G. 1944, *AJ*, **51**, 61
- van Dokkum, P. G. 2001, *PASP*, **113**, 1420
- van Maanen, A. 1940, *ApJ*, **91**, 503
- Virtanen, P., Gommers, R., Oliphant, T. E., et al. 2020, *NatMe*, **17**, 261
- Wildi, F., Blind, N., Reshetov, V., et al. 2017, *Proc. SPIE*, **10400**, 1040018
- Wright, J. T., & Eastman, J. D. 2014, *PASP*, **126**, 838
- Zapatero Osorio, M. R., Martín, E. L., del Burgo, C., et al. 2009, *A&A*, **505**, L5